Neuronal Network of *C. elegans*: from Anatomy to Behavior

A Dissertation Presented

by

Beth Li-Ju Chen

Beckman Graduate Student

to

The Watson School of Biological Sciences

at

Cold Spring Harbor Laboratory

in Partial Fulfillment of the Requirements

for the Degree of

Doctor of Philosophy

in

Biological Sciences

Cold Spring Harbor Laboratory

April 2007

Acknowledgements

I would like to first thank my research advisor, Mitya Chklovskii, for the original ideas of this thesis. I am grateful for his support, encouragement, and guidance through the various twists and turns of the project, especially the opportunity to perform laboratory experiments despite of being in a computational group.

For the electron micrograph reconstruction project, I would like to acknowledge David Hall from Albert Einstein College of Medicine and members of his lab: Zeynep Altun and Robyn Lints. I am grateful for Dave's generosity in allowing me to freely comb through the delicate prints and notebooks. I also appreciated the time Dave took in teaching me the basics of *C. elegans* biology.

Jon Pierce-Shimomura was the person who initiated the project of imaging *C. elegans* muscles along with Jami Dantsker. Jon's idea paved the way to the latter half of this thesis. I only hope he will get as much out of this collaboration as I have. I am indebted to Cori Bargmann for allowing me to perform calcium imaging experiments in her lab at Rockefeller University. She has been generous with her time, lab space, equipment, resources, and provided valuable advice throughout the project. In addition to everyone in Cori's lab, I would like to especially acknowledge Manuel Zimmer. Manuel taught me everything in the lab from worm rearing to imaging to molecular biology. I am thankful for his patience, diligence, and thoughtful comments.

I also want to acknowledge current and former members of the Chklovskii lab (Yuriy Mishchenko, Max Reigl, Armen Stepanyants, Sen Song, Quan Wen) for their comments and ideas.

Finally, I want to thank my husband, Pavel, and daughter, Madeleine, for their patience and support.

The Beckman Graduate Studentship from the Watson School of Biological Sciences funded this work.

Table of Contents

Chapter 1: Introduction

For many of us in the field of neuroscience, our ultimate objective is to understand human behavior from a biophysical perspective. To study the neural correlate of behavior, we must understand the structure of the brain and what changes affects behavior. The nervous system consists of a network of neurons organized and connected in a highly specified manner. Functional properties of the system, and thus behavior, depend critically on the characteristics of this complex structure.

However, the task of understanding behavior from the neuronal network is daunting on multiple levels. The mammalian brain consists of hundreds of billions of neurons, each with thousands of connections (Braitenberg and Atwood 1958). The sheer size of the mammalian nervous system makes construction of a detailed wiring diagram near impossible. Furthermore, neuronal connections in the brain can change as an animal develops and encounters different environmental stimuli. To establish a predictable link between behavior and neural anatomy, we need to work in a model system that exhibits a set of standard behaviors and has a relatively stable neuronal circuitry.

For this task, we turn to a small, seemingly simple organism, the soil-dwelling worm, *Caenorhabditis elegans*. The adult hermaphrodite worm is approximately 1 mm in length and 80 μm in diameter. Out of the 959 somatic cells, 302 are neurons connected by about 10,000 synapses (White et al. 1986; Durbin 1987). Although not fully characterized, the wiring diagram and the location of neuronal cell bodies have been well studied and found to be fairly reproducible from animal to animal (White et al. 1986). Despite the simplicity of the nervous system, the worm possesses a set of stereotypical behaviors: head movements, forward and backward locomotion, and turns (Croll 1975). When presented with external stimuli, the worm exhibits characteristic responses such as chemotaxis, thermotaxis, osmotic avoidance, and mechanosensory responses (Chalfie and White 1988).

Much to the credit of Sydney Brenner, *C. elegans* is an extensively studied model organism in biology. In 1963, Brenner, in search of a multi-cellular system for the study of development and

the nervous system, selected the microscopic nematode for its size, ease of cultivation, and short life cycle (Brenner 1988). Over the years, a wide range of behavioral and morphological mutants have been isolated and characterized. Through the mapping of the *C. elegans* genome, the worm community have been afforded with a collection of genetic markers and tools (Ambros 2006). The worm is also a favorite organism for neuroscientists due to the array of techniques available for probing the nervous system at a single cell or even finer level. Using focused laser light, individual neurons or even portions of neuronal projections can be eliminated without damaging other parts of the worm (Sulston et al. 1983; Yanik et al. 2004). In the last 10 years, researchers have developed whole-cell patch clamp preparations for recording electrical properties of single neurons and a primary cell culture system for *in-vitro* studies (Goodman et al. 1998; Christensen et al. 2002). Most recently, genetically encoded calcium indicators have been used to successfully measure calcium concentration changes in muscles and neurons in behaving worms (Kerr et al. 2000; Suzuki et al. 2003).

In the current work, we perform laboratory experiments and computational modelling to relate neuronal connectivity to neuron function and animal behavior in the aforementioned simple and well-described model system, the nematode *Caenorhabditis elegans*. This study is divided into three parts: 1. Reconstruction of the *C. elegans* neuronal system; 2. Wiring optimization can relate neuronal structure and function; 3. How do worms move?

First, to predict behavior from neural structure, we need to start from a comprehensive description of the full neuronal network. The wiring diagram of the worm nervous system, although well documented, is not complete, especially connectivity in the mid-body of the worm. In Chapter 2, we present a more complete and updated version of the *C. elegans* nervous system than what is currently available. The work is a consolidation of previously published and unpublished data from White *et al.* (White et al. 1976; White et al. 1986). In collaboration with David H. Hall at the Albert

Einstein College of Medicine, we fill gaps in the wiring diagram using new electron micrographs from the original thin worm sections (White et al. 1976; White et al. 1986).

Second, since neural function is intimately linked to its structure, we study the physical design rules that govern the organization of neurons in the worm in an effort to infer function. In Chapter 3, we compute the optimal placement of neurons through minimization of wiring. The results provide insights for understanding the constraints imposed on the system and related network function.

Third, we use the updated wiring diagram from Chapter 2 to predict locomotive patterns intrinsic to the *C. elegans* neuronal circuitry. In Chapter 4, we begin with a study of worm directed forces during locomotion by performing calcium imaging of body wall muscles. Then, using a linear model, we explore the dynamic properties of the worm locomotive circuit. The results of the computational models are compared to the pattern of activity observed from imaging experiments.

Chapter 2: Reconstruction of the *C. elegans* Neuronal System

2.1 Introduction

For the past three decades, researchers from multiple laboratories have undertaken the daunting task of mapping the *C. elegans* nervous system (Ward et al. 1975; Ware et al. 1975; White et al. 1976; White et al. 1986; Hall and Russell 1991). These efforts involved the painstaking work of reconstructing neurons from electron micrographs (EM) of 50 nm thin worm sections. Despite the time and efforts put into these studies, the wiring diagram remained incomplete.

Three main aspects of the published works still need to be addressed: 1. Majority of the motor neurons located in the mid-section of the worm body (58 out of 75) did not have published reconstructions. 2. The connectivity of neurons in the published literature was specified at different levels. Connections in the nerve ring were sketched out by position of each synapse. Connections in other parts of the worm, on the other hand, were specified by neuron class, combining data of bilateral neurons into one with no information on synapse location. 3. The published data was not self-consistent. Over 20% of the recorded synapses had mismatched or missing reciprocal connections. For example, Neuron A was recorded to send a synapse to Neuron B but Neuron B was not noted to receive synapses from Neuron A.

In 1986, for his doctoral thesis, Durbin revisited the EM prints used in White's Mind of the Worm (M.O.W.) and noted substantial updates to the published connectivity data in the anterior portion of the worm (White et al. 1986; Durbin 1987). This version of the wiring diagram was self-consistent with synapses specified by neuron, partner neuron, synapse type, synapse number, and the animal used for the reconstruction. Unfortunately, neurons with cell body behind the pharynx of the worm were excluded from this database. Furthermore, the reconstructions did not end at a common place on the worm body for each neuron. Some connectivity data went no posterior than the RVG (retro-vesicular ganglion) while others included synapses in the ventral cord of the worm (White et al. 1986).

Another group of researchers, Achacoso and Yamamoto (AY), also made attempts to remedy the issues inherent in the published data with their version of the worm wiring diagram (Achacoso and Yamamoto 1992). Holes in neuron reconstructions were filled by extrapolations and inferences from synaptic connections of similar neurons, and educated guesses. Connections were specified at the neuron-to-neuron level. The wiring diagram was rendered self-consistent by forcing non-symmetric connections to take on the maximum number of synapses recorded by a given neuron pair. For example, if Neuron A was specified to send 3 synapses to Neuron B but Neuron B was specified to receive only 2 synapses from Neuron A, then the number of synapses Neuron B receives from Neuron A was changed to 3. Since the work did not incorporate new data from experiments, AY's wiring diagram was no more complete than data published in previous works.

For the current work, we compiled an updated, more complete version of the wiring diagram (280 non-pharyngeal neurons, excluding 2 canal associated CANL/R cells) using both published and unpublished wiring data as well as brand new reconstructions derived from White and co-workers' original thin worm sections (White et al. 1986).

2.2 Results and Discussion

2.2.1 Updated Connectivity

The new version of the wiring diagram incorporates original data, new reconstructions, as well as updates based upon later work (Hobert, O. & Hall, D. H., *unpublished* (1999), and Durbin, R. M., *unpublished* , http://elegans.swmed.edu/parts/neurodata.txt (1986)). Over 3000 connections, including chemical synapses, electrical junctions, and neuromuscular junctions were added and/or updated from the previous version.

In the mid-section of the worm, all 75 motor neurons were either complete or partially reconstructed from electron micrographs. Connectivity was specified between neuron pairs. Inconsistencies within the data were reconciled by checking against original EM and handwritten

notes from White and co-workers. Due to rather sparse sampling of data along lengths of the sub-lateral, canal-associated lateral, and mid-body dorsal cords, connectivity ambiguities for a select few neurons remain (White et al. 1986; Hall and Russell 1991). We made no attempts to "fill" these ambiguities with extrapolations from existing synapses. The wiring diagram of 280 non-pharyngeal neurons in *C. elegans* is now 97% complete, covering 6393 chemical synapses, 890 electrical junctions, and 1410 neuromuscular junctions (Fig. 2.1).

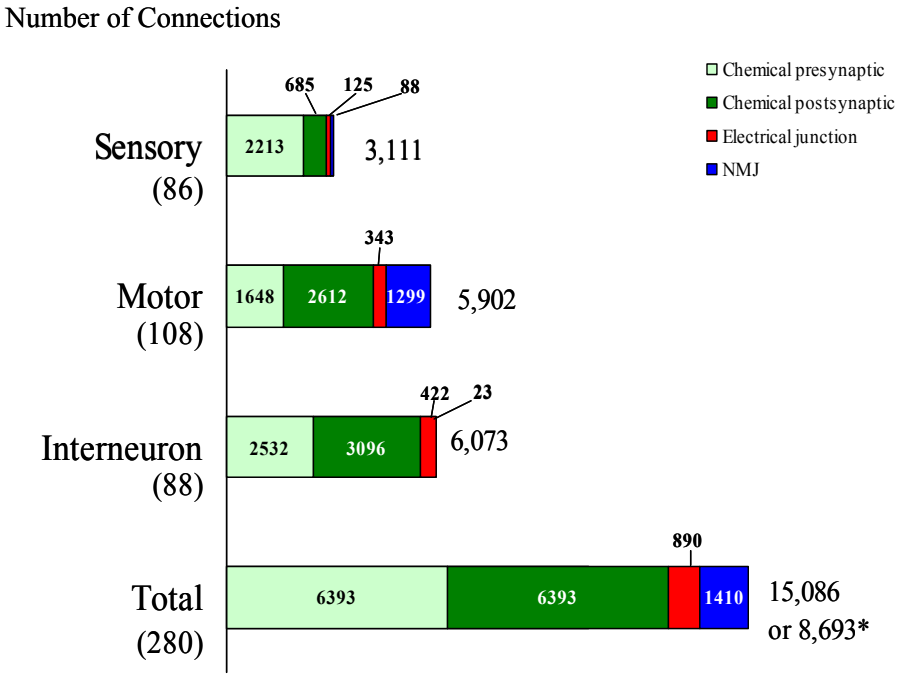

Figure 2.1: Updated wiring diagram for non-pharyngeal neurons, canal associated cells (CANL/R) excluded. The number of connections for each type of synapse (chemical, electrical and neuromuscular junction (NMJ)) is listed by neuron type. The number in parentheses below each neuron type indicates the number of neurons. *Total value tabulated by counting pre- and post-chemical synapses as a single synapse.

In the current wiring diagram, 24% of connections are either new or updated from the previously published version**.** The changes consist of 65.7% chemical synapses, 12.2 % electrical junctions and 22.1% neuromuscular junctions (Fig. 2.2). Most of these changes (89.6%) are new data

from previously unpublished ventral cord motor neurons. Although White's wiring diagram showed only 17 out of the 75 motor neurons in the ventral nerve cord, we believe White provided good representatives for each class of neurons. Nevertheless, White's published work did not capture all types of connections seen in the updated version of the wiring diagram. The remaining 10.4% of updates are from neurons in the nerve ring and tail. These changes reflect mostly adjustments made to render the wiring diagram self-consistent, as described earlier.

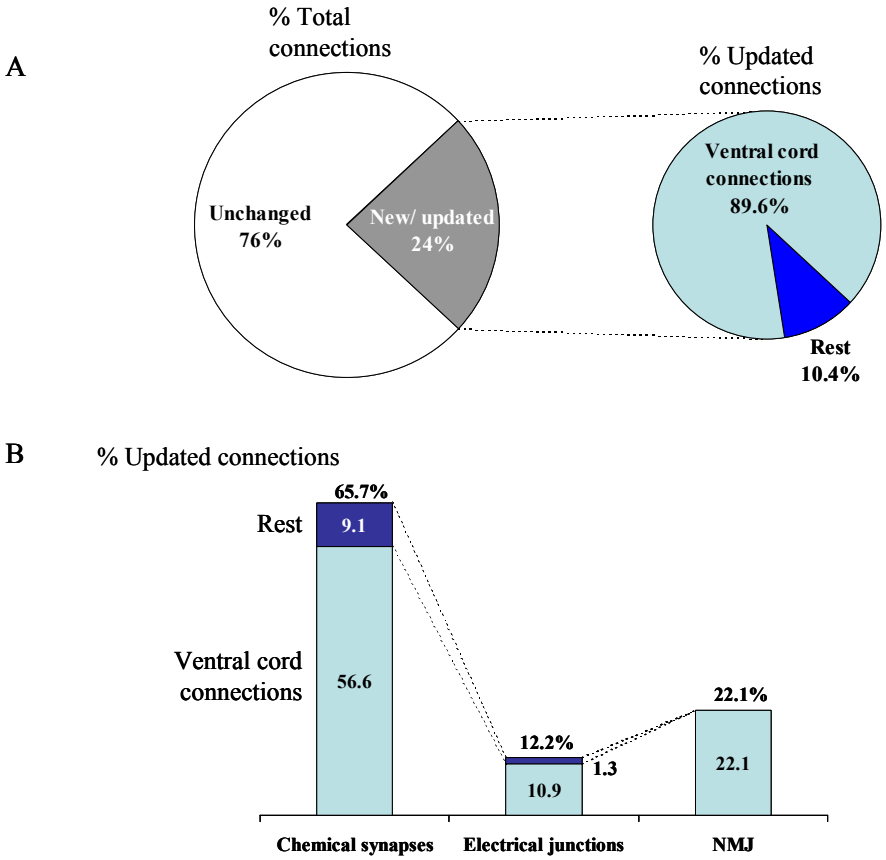

Figure 2.2: Changes in the updated wiring diagram compared to White's published version (White et al. 1986). **A.** Percent of new and updated connections in the current wiring diagram by neuron type. **B.** Percent of updated connections by synapse type.

2.2.2 Wiring Ambiguities

Several areas of ambiguity remain in the updated wiring diagram. First, due to technical constraints, wiring data of the worm was obtained from serial sections of 4 animals, 3 hermaphrodites

and 1 male (Fig. 2.3). The difficulty of tracing neural processes across different animals contributed much of the ambiguity in the mid-body and posterior regions of the worm. Appendix 2 in M.O.W. lists neurons affected in this context: DVB, DVC, ALA, CANL/R, PVDL/R, PVWL/R, PVNL/R, PQR, and PVT (White et al. 1986). Visualization of individual neurons using green fluorescent protein (GFP) reporters later confirmed assignments of ALA, PQR and noted the possible switch between processes of PVT and DVB in the anterior half of the worm. We have excluded CANL/R from our updated wiring diagram because no synapses have been found for these neurons. In addition to the above neurons, reconstruction of several motor neurons in the ventral cord required combining data from 3 animals (Fig. 2.3), raising doubt to the completeness in the reconstruction of VA10-11, VB7, VB10-11, and VC6.

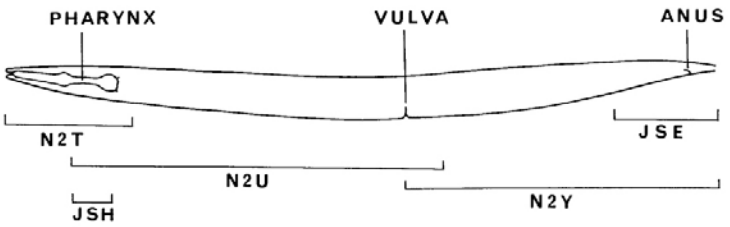

Figure 2.3: Regions of the worm covered by different reconstructed animals (cf. Fig. A1 in (White et al. 1986)). The wiring data is primarily derived from animals N2U and JSE, both adult hermaphrodites. Area anterior to the nerve ring is covered with N2T (also an adult hermaphrodite) and the gap between N2U and JSE is covered by N2Y, an adult male. JSH, and L4 hermaphrodite larva, was used only as a check of neck ring connectivity.

In *C. elegans*, chemical synapse on an electronic micrograph is characterized by dark staining of the presynaptic site (White et al. 1986). Since no specialization marks the postsynaptic element, the actual target of the synapse can be ambiguous. In the wiring data, the post-synaptic target is designated by the element's physical proximity to region of pre-synaptic density. Although a single target can usually be identified, sometimes two or three elements share the space opposite to the presynaptic density (Fig. 2.4). Under these circumstances, all potential targets of the synapses are included in the connectivity database, flagged as "receive multiples". These dyadic and triadic

synapses are thought to be functional due to the stereotypical manner in which they appear between certain classes of neurons.

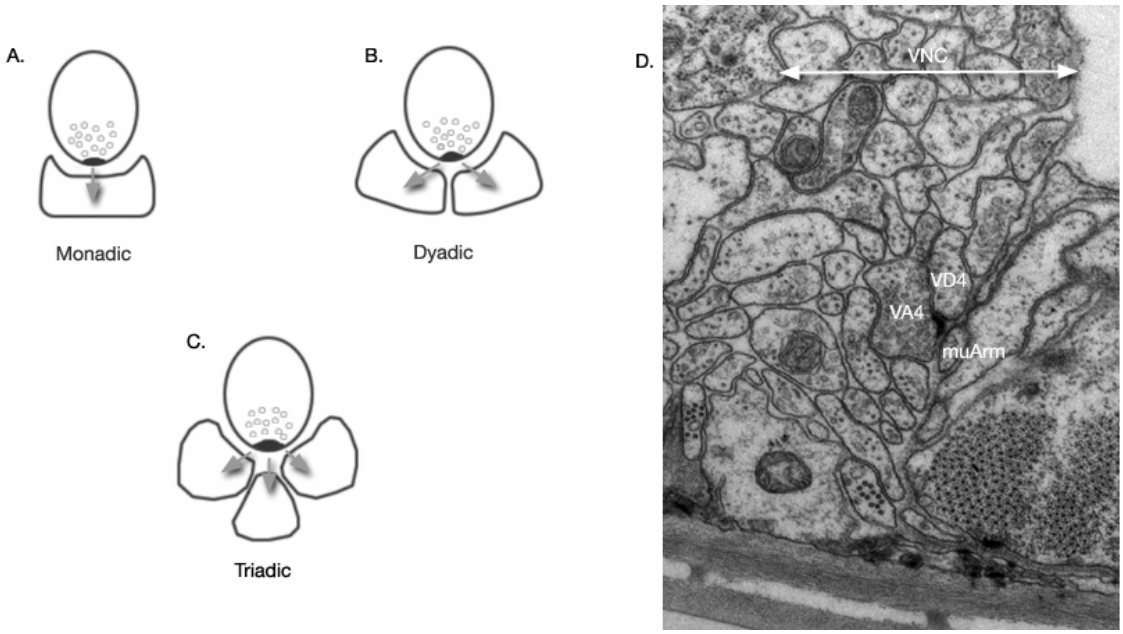

Figure 2.4: Neurons with multiple synaptic partners. Postsynaptic partners can include other neurons, muscle arms (muArm) and rarely hypodermis (synapses onto hypodermis are not included in this dataset analysis). (A) A synapse with one postsynaptic partner. (B,C) Polyadic synapse types. (D) A dyadic synaptic site on electromicrograph (White et al. 1986). The pre-synaptic neuron VA4 appears directed towards both VD4 and a muscle arm (figure created by Zeynep Altun).

Quite unlike chemical synapses, electrical junctions appear as flat, darkly stained cell membranes between two closely apposed cells. These features are subtle and easy to misinterpret. In the wiring diagram, signatures of an electrical junction between two cells must be evident across multiple serial sections to be counted. The stricter criteria used for scoring electrical junctions results in more potentially missed electrical synapses compared to chemical synapses.

2.2.3 Remaining Data Gaps

In the region posterior to the vulva, the scarcity of high power EM's on the dorsal side affects the reconstruction of 39 neurons. Neurons AS11, DA9, DB7, VD11-13, RID, PDA, PDB have partial dorsal data whereas AS7-10, DA7-8, DB5-6, DD4-6, VD7-10 are completely void of dorsal

reconstructions. All neurons with processes in the sublateral nerves have incomplete reconstructions. Unlike the ventral and dorsal cords, the sublateral cords were never examined under high power magnification and, therefore, never fully reconstructed.

2.3 Methods

The work in this Chapter was done in collaboration with David H. Hall at Albert Einstein College of Medicine (AECOM).

2.3.1 Compilation of Connectivity Data

We began assembling the wiring diagram by consolidating existing data from both published and unpublished sources. Using White's Mind of the Worm (M.O.W.) as the starting point, we extracted wiring data from diagrams, figures, tables, and text (for example, see (White et al. 1986) Appendix A, pages 118-122 on neuron AVAL/R). Connectivity of each neuron, its synaptic partner, synaptic type (chemical, electrical, neuromuscular) was manually entered into an electronic database. In the ventral cord of the worm, this level of synaptic specification was complicated by the fact that connections were recorded by neuron class. For example, bilateral neurons PVCL and PVCR were simply listed as PVC. We were able to assign proper connections to the appropriate left/right neuron by referring to White and coworker's original lab notebooks and original electron micrographs. In some cases, the number of synapses for a given neuron class in M.O.W. differed from the sum of connections for the bilateral pairs in the notebooks and/or EMs. The synaptic value of these neurons was determined by appropriating the value in M.O.W. according to proportionality from the notebooks/EMs.

From here, we incorporated Durbin's data, which were applicable to the anterior portion of the worm, reconstructed from the N2U animal (Durbin 1987). For neurons that projected beyond the

neck ring, only the anterior connections needed to be updated. Since data from M.O.W. did not specify location of synapses, integration proved difficult. For these neurons, we obtained positional information by cross referencing Durbin's data against original electron micrographs and his handwritten annotations in White's lab notebooks. Only synapses located in regions addressed by Durbin were included. Connections in the middle and tail regions of the worm were mostly unaffected by these updates.

With the advent of GFP reporters, researchers are able to visualize the neuroanatomy of individual neurons. These studies mostly confirmed the EM reconstructions described in M.O.W. A few differences between GFP stained neurons and White's work were observed (Hobert, O. & Hall, D. H., *unpublished* (1999). Notably, the anterior processes of DVB and PVT could have been mistakenly switched in M.O.W (White et al. 1986). Based on these findings, we reversed the connections for neurons DVB and PVT anterior to the vulva.

2.3.2 Reconstruction of Ventral Cord Neurons

Most published works have focused in the neck and tail regions of *C. elegans*, where the majority of neuron cell bodies reside. Reconstructions of neurons in the mid-body of the worm, on the other hand, are scant and incomplete. From a combination of published works ((White et al. 1976; White et al. 1986; Durbin 1987; Hall and Russell 1991), we found that wiring data for 64 neurons have large gaps or missing entirely. 61 of these are motor neurons in the ventral cord. Two are excretory neurons (CANL/R) that do not appear to make any synapses. The remaining neuron, RID, is the only process that extends the length of the animal in the dorsal cord.

At the *C. elegans* archive (AECOM), we uncovered a large number of reconstruction records in White and coworker's lab books. These notebooks identified neurons by different color code labels depending on the animal, the location of the neurite (ventral or dorsal), and magnification of the electron micrograph. To ascertain the identity of the neurons, we relied on a combination of color

code tables and comparisons of common anatomical structures between EM prints. In the end, we identified notes for full reconstructions of 24 of the aforementioned neurons. Partial connectivity data (details discussed in the following section) for the remaining 38 were also available where 22 neurons have partial/missing dorsal side connections and 6 neurons have partial ventral side connections. We checked the connections of all (both published and unpublished) neurons in the ventral cord against electron micrographs used by White and coworkers. Over 600 updates were made to the original notes and published reconstructions. Many of these updates were additions of previously missed neuromuscular junctions between ventral cord motor neurons and body wall muscles.

While conducting this work, we found that a large section of the worm on the dorsal side, from just anterior to the vulva to the pre-anal ganglion, was never photographed at high power magnification under the electron microscope. This lack of EM prints was the reason why so many neurons were missing dorsal side reconstructions. Using original thin sections for the N2U worm prepared by White and coworkers, we took new high power electron micrographs of this dorsal region. Due to the condition of the sections, only one of every 2-3 section was photographed. These new EM's extended nearly 9 μm on the dorsal side. New dorsal side data for 3 neurons (DA5, DB4, DD3) were obtained from these electron micrographs. Resource constraints prevented us from covering the entire dorsal gap.

2.3.3 Reconciliation of Synapses

The wiring diagram is considered self-consistent under the following criteria: 1. A record of Neuron A sending a chemical synapse to Neuron B must be paired with a record of Neuron B receiving a chemical synapse from Neuron A. 2. A record of electrical junction between Neuron C and Neuron D must be paired with a separate record of electrical junction between Neuron D and Neuron C. From our compilation of wiring data, including new reconstructions of ventral cord motor neurons, we applied the above criteria to isolate neurons with mismatched reciprocal records. The

discrepancies were reconciled by checking against electron micrographs and White and coworker's lab notebooks. Connections in the posterior region of the animal were also cross-referenced with reconstructions published by (Hall and Russell 1991). Reconciliation involved 561 synapses for 108 neurons (49% chemical "sends", 31% chemical "receives", and 20% electrical junctions).

Chapter 3: Wiring Optimization can relate neuronal structure and function

This chapter is a reprint of the manuscript and supplement of "Wiring Optimization Can Relate Neuronal Structure and Function" by Beth L. Chen, David H. Hall and Dmitri B. Chklovskii published in Proceedings of National Academy of Sciences (PNAS), vol. 103, no. 12, pages 4723-4728 (March 21, 2006). The subheadings and references of the original paper have been reformatted to fit with the overall structure of this thesis.

3.1 Summary

We pursue the hypothesis that neuronal placement in animals minimizes wiring costs for given functional constraints, as specified by synaptic connectivity. Using a newly compiled version of *C. elegans* wiring diagram, we solve for the optimal layout of 279 non-pharyngeal neurons. In the optimal layout, most neurons are located close to their actual positions suggesting that wiring minimization is an important factor. Yet, some neurons exhibit strong deviations from "optimal" position. We propose that biological factors relating to axonal guidance and command neuron functions contribute to these deviations. We capture these factors by proposing a modified wiring cost function.

3.2 Introduction

As brain structure is intimately related to its function, understanding structure should provide important clues to brain function. Traditionally, structural features of the brain are explained from the perspective of development, a complex process including such events as cell migration (Chalfie 1993; Culotti and Merz 1998), axonal guidance (Wadsworth and Hedgecock 1992; Tessier-Lavigne and Goodman 1996; Dickson 2002), cellular signalling (Fukata et al. 2003) and synaptogenesis (Ackley and Jin 2004; Cline 2005; Hobert 2005; Jin 2005). Although much progress has been made in understanding the mechanisms of neural development, many unanswered questions remain. In

particular, it is not known what determines the placement of neurons and synapses in the body, a question to be addressed in this paper.

Our approach for understanding neuronal structures complements neural development and relies on the existence of general principles governing the architecture of a mature brain. Specifically, we exploit the wiring economy principle proposed by Cajal more than a hundred years ago (Ramón y Cajal 1899). This principle postulates that, for a given wiring diagram, neurons are arranged in an animal to minimize the wiring cost. The evolutionary "cost" can be attributed to factors such as: wire volume (Mitchison 1991; Cherniak 1992; Chklovskii 2004b), signal delay and attenuation (Rushton 1951; Rall et al. 1992; Wen and Chklovskii 2005), as well as metabolic expenditures associated with signal propagation and maintenance (Laughlin et al. 1998; Attwell and Laughlin 2001). Although the exact origin of the wiring cost is not known, the farther apart two neurons are, the more costly is the connection between them. The wiring cost can therefore be expressed as a function of distance between neurons and consequently minimized (Mitchison 1991; Cherniak 1994; Cherniak 1995; Chklovskii 2000b; Chklovskii 2000a; Chklovskii and Koulakov 2000; Chklovskii and Koulakov 2004).

Despite many successful applications of the wiring minimization principle (Mitchison 1991; Cherniak 1992; Cherniak 1994; Cherniak 1995; Chklovskii 2000b; Chklovskii 2000a; Chklovskii and Koulakov 2000; Klyachko and Stevens 2003; Chklovskii 2004a; Chklovskii 2004b; Chklovskii and Koulakov 2004) [but see (Young and Scannell 1996)] it has never been tested on the level of individual neurons for an entire nervous system. Such testing was precluded by the lack of wiring diagrams and by the computational complexity of the optimization problem. Previous works have shown that wire length minimization can explain the layout of small systems by tabulating the amount of wire required for every possible permutation of components in the network. The actual ordering of ganglia in *C. elegans* (Cherniak 1994) and the arrangement of areas in the prefrontal cortex in the macaque (Klyachko and Stevens 2003) was found in this manner to have the shortest total wiring. Unfortunately, this brute force method is impractical for all but the smallest networks (number of components of order 10) because the number of permutations increases exponentially with the

number of components. In addition, the results provide only the relative ordering of components and not their exact positions in an actual animal.

In this paper, we solve for the neuronal layout of an entire nervous system of the nematode *C. elegans* using the updated wiring diagram and powerful placement algorithms borrowed from computer engineering (Hall 1970; Weis and Mlynski 1987; Sigl et al. 1991; Tsay and Kuh 1991; Kennings and Markov 2000). We consider 279 neurons (pharyngeal and unconnected neurons excluded) of the hermaphrodite worm, whose identity, locations of cell bodies, sensory endings and neuro-muscular junctions (NMJ), as well as the wiring diagram have been well-studied and found to be largely reproducible from animal to animal (White et al. 1986; Hall and Russell 1991). The length of the worm is more than ten times greater than its diameter, allowing us to reduce the problem into one dimension.

By minimizing cost of connecting the nervous system, our solution predicts the position of most neurons along the anterior-posterior (AP) body axis of the nematode worm. This result suggests that wiring minimization is a good general description of the relationship between connectivity and neuron placement. A comparison of the cost-minimized layout with actual neuron positions revealed groups of outlier neurons with distinct structural characteristics. Interestingly, neurons within each group have been shown in experiments to play similar roles in the worm nervous system: developmental pioneering and signal integration for motor control. We suggest that the results obtained from cost minimization can be used in a number of ways to infer neuron function.*

3.3 Results

3.3.1 Wiring Cost Minimization in the Dedicated-Wire Model

We start by modelling the nervous system (see Figure 3.1B inset for example) as a network of nodes that correspond to neuronal cell bodies, connected by wires that represent synapses (Figure 3.1C inset). We call such model "dedicated-wire" because each synapse has its own wire. Additional wires connect neurons to sensory endings and muscles. Assuming that the placement of these structures is subject to constraints independent of neuronal organization, their positions are fixed.

The total wiring cost (C^{tot}) can be expressed as the sum of an internal cost to connect neurons to each other, (C^{int}), and an external cost to attach neurons to the fixed structures (C^{ext}):

$$C^{tot} = C^{int} + C^{ext} . \tag{3.1}$$

We assume that the cost of wiring i^{th} and j^{th} neuron is proportional to some power, ζ, of the distance between them. Then the total internal wiring cost is:

$$C^{\text{int}} = \frac{1}{2\alpha} \sum_i \sum_j A_{ij} \left| x_i - x_j \right|^{\varsigma} , \tag{3.2}$$

where x_i is neuron position and α is an unknown coefficient to be discussed later. A_{ij} is an element of the adjacency matrix A, representing the total number of synapses between neurons i and j in both directions. As the wiring cost is assumed to be independent of the directionality of synapse (i.e. signal propagation from neuron i to j or vice versa) matrix A is symmetric ($A_{ij} = A_{ji}$). Also, the cost is assumed to be independent of synapse polarity (i.e. inhibitory vs. excitatory) so the adjacency matrix is non-negative ($A_{ij} \geq 0$).

The second term in Equation 3.1 represents the cost of wiring neurons to sensory organs, k, located at positions s_k, and muscles, l, at positions m_l:

$$C^{ext} = \sum_i \sum_k S_{ik} \left| x_i - s_k \right|^{\varsigma} + \frac{1}{\alpha} \sum_i \sum_l M_{il} \left| x_i - m_l \right|^{\varsigma} \tag{3.3}$$

where S_{ik} is the number of synapses between neuron i and sensory organ k and M_{il} is the number of synapses between neuron i and muscle l . In the schematic network illustrated in the inset of Figure 3.1C, the adjacency matrix (A), neuron-to-sensory (S) and neuron-to-muscle matrices (M) are:

$$A = \begin{pmatrix} 0 & 3 & 1 \\ 3 & 0 & 1 \\ 1 & 1 & 0 \end{pmatrix}, \; S = \begin{pmatrix} 1 \\ 0 \\ 0 \end{pmatrix}, \; M = \begin{pmatrix} 0 \\ 0 \\ 1 \end{pmatrix} \tag{3.4}$$

To account for multiplicity of synapses on a single neurite, we apply a coefficient $1/\alpha$ to neuron-to-neuron (Eq. 3.2) and neuron-to-muscle (second term in Eq. 3.3) costs based on the following. In the dedicated-wire model, the cost of connecting two neurons is directly proportional to the number of synapses between them (Figure 3.1C, inset), equivalent to having a dedicated wire for each synapse. Yet, in the actual worm, the majority of neurons are non-branching and bipolar, making an average of 58.6 *en passant* synapses and neuromuscular junctions with only two neurites (or two wires). This morphology can be taken into account by normalizing each neuron-to-neuron and neuron-to-muscle connection by the average number of synapses per neurite (α = 29.3 or 58.6 synapses per neuron divided between 2 neurites). Sensory neurons, on the other hand, typically send one specialized neurite to the sensory organ (White et al. 1986), which, with a few exceptions, does not make synapses with other neurons or muscles. Thus each sensory fixed point, by construction, connects to a neuron through a dedicated wire and needs not be normalized. An alternative way to incorporate this neuronal morphology is by using a "shared-wire" model (Figure 3.1E, inset) which will be introduced later.

We find the optimal neuronal placement that minimizes the wiring cost-function defined by Equations (3.1-3.3). Initially, we assume that the cost of connecting two neurons increases as the square of the distance between them (ζ =2 in Equation 3.2 and 3.3). The quadratic cost function can be minimized analytically and the position of neuronal cell bodies is given by (Hall 1970; Tsay and Kuh 1991; Chklovskii 2004a) where δ_{ij} is the Kronecker delta:

$$x = Q^{-1}\left[Ss + \frac{1}{\alpha} Mm \right]$$
$$Q_{ij} = \delta_{ij}\left(\frac{1}{\alpha}\sum_p A_{ip} + \sum_k S_{ik} + \frac{1}{\alpha}\sum_l M_{il} \right) - \frac{1}{\alpha} A_{ij} \qquad (3.5)$$

Minimization of the quadratic cost-function is mathematically identical to finding the equilibrium placement of objects connected with elastic rubber bands (minimum elastic energy of rubber bands with zero length at rest).

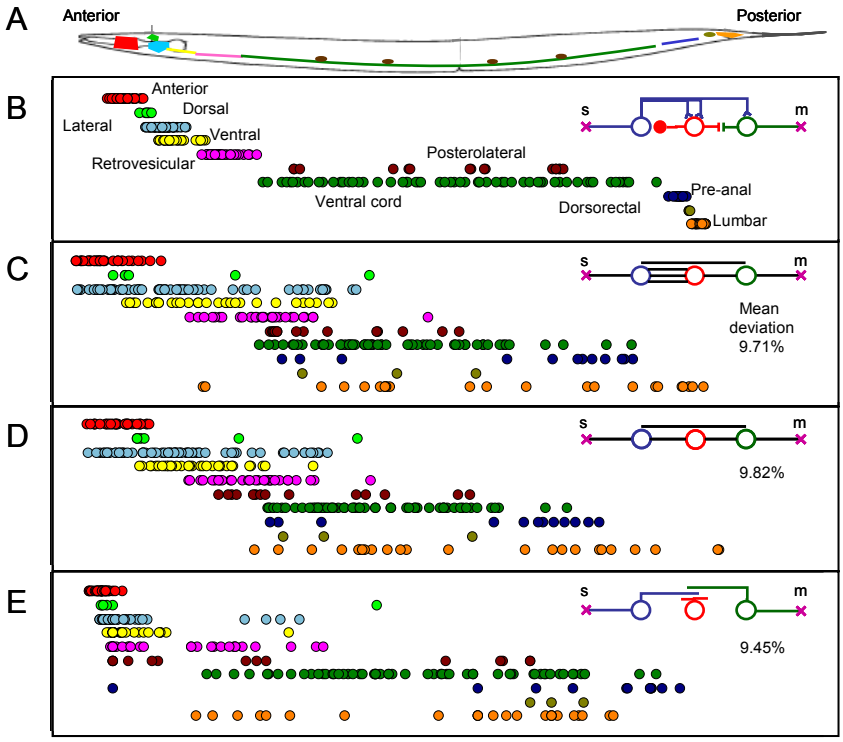

Figure 3.1: Actual and predicted neuronal cell body positions. **A.** Neuronal layout in the worm, pharyngeal neurons excluded. Each color denotes a ganglion. **B.** Actual placement of neuronal cell bodies projected onto AP axis. Circles of the same color represent cell bodies belonging to the same ganglion. Plots for each ganglion are offset vertically to aid the eye. Inset: Schematic example of biological network of three neurons and two fixed points: s= sensory ending; m=muscle. Blue neuron is bipolar with one neurite attaching to the sensory ending and the other making two excitatory synapses onto the red neuron and one excitatory synapse onto the green neuron (circle represents the cell body). The red neuron makes an inhibitory synapse onto the blue neuron (line ending in circle) and a gap junction (bar) with the green neuron. The green neuron has a neuromuscular junction. **C.** Neuronal layout predicted from minimization of quadratic wiring cost in dedicated-wire model. Inset: Weighted dedicated-wire model. Each black line or wire corresponds to one synapse independent of polarity (excitatory vs. inhibitory), directionality or modality (chemical vs. gap). **D.** Neuronal layout predicted from the binary dedicated-wire model. Inset: Binary dedicated-wire model. Each wire corresponds to a synaptic connection neglecting multiplicity of synapses. **E.** Neuronal layout predicted from the shared-wire model. Inset: Shared-wire model. Neurons represented as non-branching wires (colored lines), which must overlap if a synaptic connection exists. Cell body location on the wire can be calculated using different rules.

3.3.2 Comparison of the Minimum-Wiring Placement with Actual Layout

Using the complete connectivity diagram of the *C. elegans* nervous system, we calculate neuron positions that minimize the quadratic cost function (ζ=2 in Eq. 3.2-3.3, $1 < \zeta < 4$ to be considered later). Figure 3.1C shows optimal neuronal layout in the one-dimensional worm, where neurons from the same ganglion are represented by the same color, offset vertically for clarity.

We compare this result to actual locations of neuronal cell bodies projected into one-dimension along the AP axis of the worm, Figure 3.1B. Neurons belonging to the same ganglia are clustered (positioned near each other) in the actual layout. Wiring cost minimization predicts somewhat more dispersed clusters of neurons located in the anterior two-thirds of the worm and no clustering for neurons in the tail ganglia (see Ganglia Distribution in Supplement). Later we will discuss possible causes for such discrepancies. Since a large number of the sensory organs are located in the tip of the head (White et al. 1986), aggregation of neurons in the anterior region of the animal is consistent with minimization of cost required to connect these sensors (Cherniak 1994). The predicted anterior-to-posterior order of the first five ganglia, as defined by the median of neuron positions, agrees with actual. The actual ganglia ordering was previously obtained by Cherniak via brute force enumeration of all possible permutations (Cherniak 1994). However, as mentioned previously, the method used to obtain Cherniak's result cannot be applied at the level of individual neurons.

Next, we plot predicted positions of individual neurons as a function of actual positions in the worm, Figure 3.2. Neuron locations in the animals are scaled between 0 and 1 where 0 is the head and 1 is the tail. The majority of neurons in the network lie along the diagonal of the plot, where predicted position equals actual position. On average, the cost-minimized neuron is located at 9.71% of the worm body length away from the actual location. Half of the predicted positions lie

within 5.10% from their actual layout. The discrepancy between the mean and median of the distribution indicates that a small number of neurons account for the largest deviations. These "outlier" neurons will be analyzed further in the following sections.

To evaluate how well wiring cost minimization predicts neuron position we compare our results against a null hypothesis that more related neurons are positioned closer to each other. In *C. elegans*, the lineages of individual cells are reproducible and have been fully mapped (Sulston and Horvitz 1977; Sulston et al. 1983). By assuming that each cell division in the lineage tree reduces "relatedness" by one unit, we found the "relatedness" matrix between any two neurons in the nervous system (see Lineage Analysis in Supplement). Then we minimized the quadratic cost function with coefficients given by the "relatedness" matrix by substituting non-existent external connection with a uniform repulsive force (Chklovskii 2004a). The mean deviation from actual is 26.1%, a worse prediction than that generated by wiring minimization.

We also evaluate how well cost minimization is able to predict neuron position by comparing our results to a neuronal layout generated at random from a uniform distribution. Randomly placed neurons have a mean deviation from the actual position 34.6% and the median of 30.9%, both much greater than wire-minimized placement. Provided the distribution of the mean is Gaussian, the probability of obtaining an average deviation for 279 neurons better than the results from cost minimization is 10^{-68}. Therefore, wiring cost minimization is a meaningful description of the relationship between neuronal arrangement and connectivity in the worm.

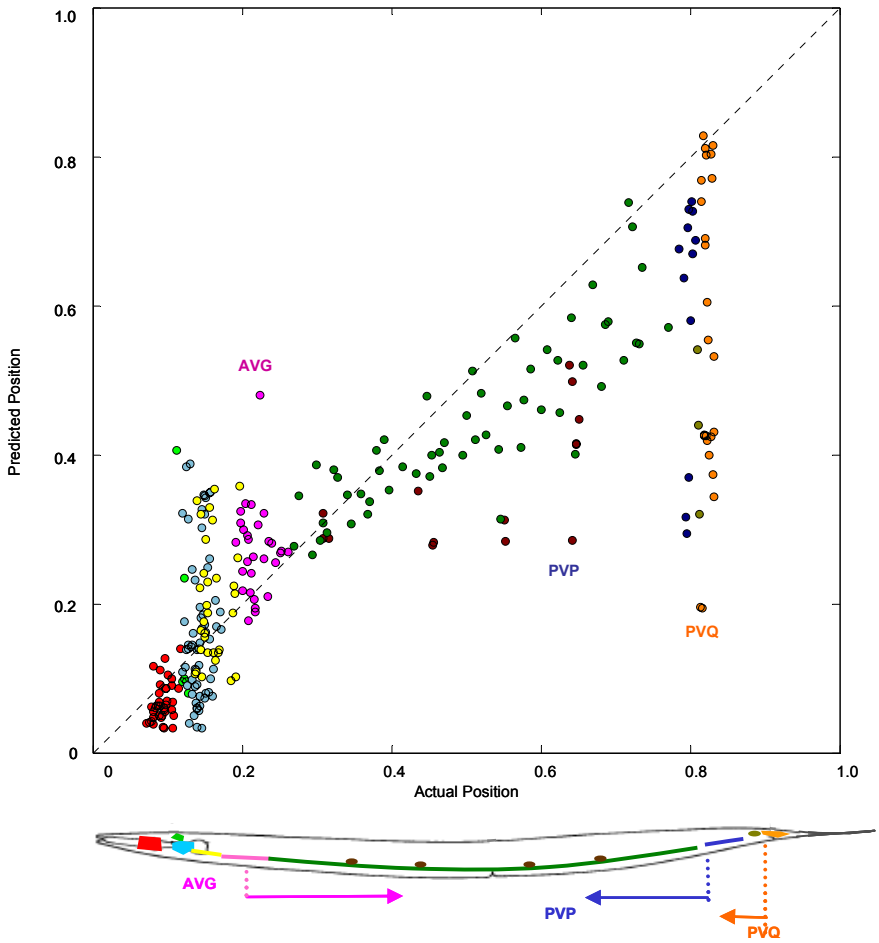

Figure 3.2: Neuron positions predicted by the quadratic dedicated-wire model versus actual neuron positions. Positions are normalized by the worm body length (0=head; 1=tail). Perfect predictions fall on the diagonal. Circles of the same color represent cell bodies belonging to the same ganglion. Three classes of pioneer neurons are labelled. Bottom: Schematics depicting the progression of pioneer neurons during worm development. Arrows indicate direction of neurite growth.

Despite reasonable agreement between predicted and actual layout, the total wiring cost of the actual network is almost four times greater than that of the optimized solution. Does this discrepancy arise from the cost of internal or external connections? The cost from neuron-to-neuron connections (C^{int} from Equation 3.1 and 3.2) make up 91.7% of total cost in the actual worm. This value is 6.24 greater than the internal cost from the predicted layout. On the other hand, the ratio of actual to predicted external costs (C^{ext} from Equation 3.1 and 3.3) is significantly lower at 0.93. This result suggests that neurons in the actual layout are well positioned to minimize connections to external structures but are not optimized for neuron-to-neuron connections.

However, the total cost of the actual placement is still four times less than that of the randomly generated placement. In other words, the total cost ratio of optimized to actual to random layout is 1:4:16. Provided the distribution of cost for a random placement is Gaussian, the probability of obtaining a cost equal or lower than the actual cost is 10^{-33}. Again, the significance of this metric suggests that the wiring minimization approach gives non-trivial results.

3.3.3 Robustness of Optimization Results to Small Variations of Parameters

To determine the robustness of the wire-minimized solution, we explored several aspects of the cost function and assessed their impact on the ability to predict neuronal layout.

First, we analyze the sensitivity of the wire-minimized layout to the normalization coefficient α and the exponent ζ. As mentioned, our cost formulation accounts for multiple synapses on a given neurite by normalizing connection weights by the average number of synapses per neurite (α=29.3). We test how the predicted layout changes by varying α between 1 and 45. Since the choice of the quadratic form of the cost function may seem arbitrary, we also varied the power of wire length in the cost function, ζ in Equation 3.2 and 3.3 between values of 1 and 4. As argued previously, wiring cost is likely to scale supra-linearly (ζ >1) with distance between neurons (Chklovskii 2004a). If so, the minimization problem is convex and can be efficiently solved numerically. The lowest mean deviation, 9.71%, is achieved by using the cost function with normalization coefficient around 27 and exponent around 2 (see General Power-Law Cost Function in Supplement). Interestingly, these values are close to those chosen from biological considerations and validate the quadratic cost function.

Second, we test the importance of synaptic multiplicity between neurons. Instead of a wire dedicated to each synapse between cells (Figure 3.1C, inset), we use a single wire to connect a given pair of neurons regardless of the number of synapses (Figure 3.1D, inset). In other words, we minimize the quadratic cost function with a binary connection matrix (only 0 or 1 elements in the matrix *A* from Eq. 3.2). Using ζ=2, the lowest mean deviation between predicted and actual position

(9.82%) is higher than the result from a synapse-number weighted cost function and was found at α=8. In the actual worm, the average number of synaptic partners (as opposed to individual synapses) per neurite is 12.2, close to the optimal value of α obtained from the binary connection matrix.

To summarize, we find that various reasonable cost functions predict neuronal placement incomparably better than the random one. Although mean deviations vary somewhat between different cost functions they are not far from the best known solution. Thus the wire length minimization approach is rather robust. As the quadratic cost function can be solved exactly and is reasonably close to the best-known solution, it may serve as the reference predicted layout. Although the predicted placement is only approximately correct, we recall that the problem was solved in one dimension. Such dimensionality reduction may introduce errors on the order of the inverse aspect ratio of the worm, just under 10%. As the mean deviations we report approach this range, wiring optimization results are encouraging.

3.3.4 What Causes Discrepancies Between Predicted and Actual Neuronal Layouts?

Several reasons may account for the deviation between positions predicted by wiring-cost minimized and actual neuron positions: 1. The actual system is not fully optimized. 2. The wiring diagram is still somewhat incomplete. 3. The wiring cost function does not fully represent costs associated with neuronal placement or constraints other than connectivity need to be taken into consideration. Although reason #1 remains a possibility, its exploration lies beyond the framework of the optimization approach (Parker and Maynard Smith 1990). Reason #2 can be addressed by future reconstructions. Here, we explore the merit of Reason #3.

By taking a closer look at neurons with the greatest deviation between predicted and actual positions, we find that these "outliers" have common morphological features. Figure 3.3A shows the histogram of differences between predicted and actual positions for neurons with cell bodies in the head, mid-body, and tail of the animal. We define the head region by positions along the body axis <25% from the anterior of the worm; mid-body is between 25% and 75%; tail is >75% (see Neuron Position in Supplement). The top 10 outliers in the network are in the neuron classes PVQ, PVT, DVC, PVN, PVP, PVW, PVC, all located in the tail of the worm. The biggest outliers in the head are AVA, AVG, and RID. In the mid-body, SDQL, HSNL and DA06 have the largest deviations. All of these neurons, except DA06, have long processes that span > 25% of the worm body.

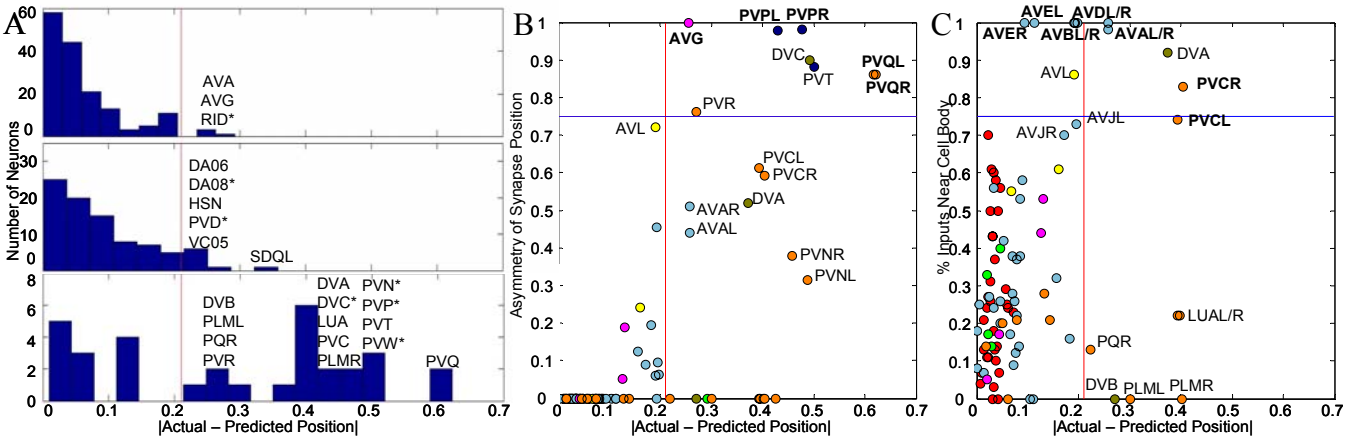

Figure 3.3: Analysis of cost-minimization outliers. **A.** Histogram of absolute value of predicted – actual positions. Top: Neurons with cell bodies in the head of the worm. Middle: Neurons with soma in the mid-body. Bottom: Neurons with soma in the tail. Red vertical line in each plot marks the first standard deviation from the mean. Star indicates neurons with ambiguous wiring (see text and Supplement for definitions) **B.** Asymmetry of synapse position relative to the soma (1 = all synapses in the head and tail are located on opposite end of the worm as the cell body; 0 = all synapses in the head and tail are close to the cell body) versus prediction error of wiring cost minimization. Bolded neurons above blue line (asymmetry > 75%) are pioneer neurons. **C.** Synaptic inputs near the cell body versus prediction error of wiring cost minimization. Bolded neurons above the blue line (%inputs > 75%) are command interneurons for locomotion. Vertical red line is first standard deviation of wiring cost model deviation.

3.3.5 Distribution of Synapse Locations Along a Neuron May Not Predict Cell Body Placement

As most outliers have long processes spanning the worm body, could the constraints for cell body placement along the process be different from the dedicated wire model? Using the quadratic wiring cost, the dedicated wire model places neuronal cell body at the weighted center of mass of the positions of its synaptic partners and fixed structures. Then, the cell bodies should not deviate too far from the center of mass location of their synapses.

We test whether actual cell body locations are consistent with synapse distribution along a neurite as expected from the dedicated-wire model. Since the position of synapses can only be approximated to within a third of the worm body (see Synapse Position in Supplement), we consider long-reaching (>25% body length) neurons with cell body located in either the head or tail (109 neurons). Using an asymmetry factor defined by the percentage of head and tail synapses located on the same end of the worm as the cell body, we study how synapses distribute between head and tail. The asymmetry factor is 0 if all synapses are at the same end of the worm as the cell body. For neurons with 100% of head and tail synapses on the opposite end of the worm as the cell body, the asymmetry factor is 1.

We find all neurons with asymmetry factor >0.75 (above blue line in Figure 3.3B) are outliers in the wiring minimized layout (right of red line in Figure 3.3B). This group of neurons include all developmental pioneers of the ventral cord currently known in *C. elegans*: AVG, PVPL/R, PVQL/R. By comparing the positional deviations of known pioneers with deviations of the rest of the neurons in the system, we find that all pioneers are outliers in the wire-minimized layout (P=0.002 from Student's t-test). The most prominent anterior outlier, AVG, is born in the head (Durbin 1987). During development, the neuron sends the first posterior–directed projection into what eventually becomes the right ventral cord, pioneering a path for other anterior neurons to follow (Figure 3.2). Along the way, AVG makes synapses with neurons in the mid-body and the tail. Neurons PVP and

PVQ, the biggest outliers in the tail, behave similarly but in the reverse direction: they are born in the tail, send pioneering processes forward. Ablation of these pioneer neurons results in disorganization of ventral cord fascicles, although a nerve cord is still formed (Durbin 1987). All of these pioneer neurons are characterized by long processes that span the entire length of the worm with the majority of synapses situated outside of the soma region.

Another key player in neural development, PVT, also has synapses mostly on the opposite end of the worm from the soma. The previously published wiring of PVT (White et al. 1986) was later amended (Hobert, O. & Hall, D. H., *unpublished* (1999)). Interestingly, only after these changes are incorporated does PVT emerge from this outlier analysis. Functionally, PVT acts as a guidepost cell for neurons located in the posterior region of the worm to grow forward (Antebi et al. 1997; Ren et al. 1999) and maintains the organization of ventral cord fascicles (Aurelio et al. 2002). Without PVT, axons in the lumbar ganglia fail to enter the ventral cord in a single bundle and axons already in the ventral cord cross the ventral midline in an aberrant manner.

The remaining neurons with asymmetry factor >0.75, DVC and PVR, are also outliers in the wire-minimized solution and, based on their structural characteristics, we propose that DVC and PVR may also play pioneering or developmental roles. PVR, an interneuron located in the lumbar ganglion, is a putative tail sensory neuron with some animals displaying microtubule bundles in the posterior process (White et al. 1986; Hall and Russell 1991). The pioneering role of DVC has been previously postulated by Durbin (Durbin 1987) using independent data. However, this hypothesis was not fully verified by experiments (Durbin 1987).

3.3.6 Directionality of Synapses Along Neuron May Bias the Location of Cell Bodies

As analysis of synapse position relative to the cell body does not account for all outliers, such as AVA and PVC where synapses are evenly distributed, we hypothesize that the directionality of

synapses might be important. We found an asymmetry in the spatial distribution of pre- and post-synaptic terminals for AVA and PVC (Figure 3.4). Specifically, the region containing cell bodies of these neurons contain more inputs or post-synaptic terminals than pre-synaptic terminals. This unexpected result suggests that the distance between cell bodies and pre- versus post-synaptic terminals invoke different connection costs. Since the dedicated-wire model does not distinguish between the location of individual synapses nor the type of synaptic terminals, the failure of our cost minimization to predict the actual position of these neurons is not surprising.

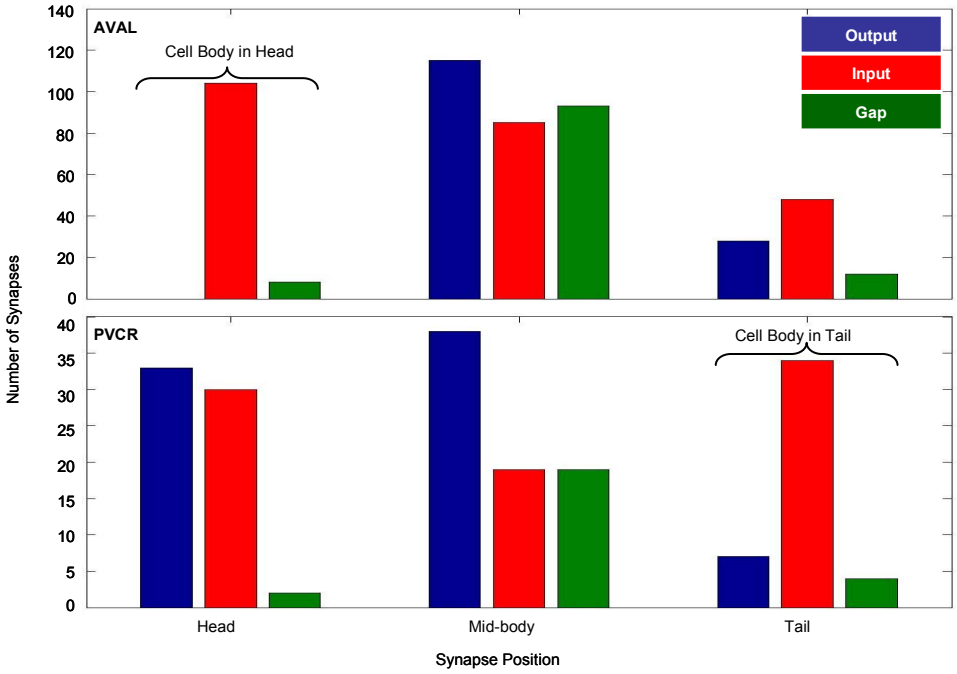

Figure 3.4: Distribution of synapses by directionality and type along command interneurons. Neuronal outputs or pre-synaptic terminals (blue), inputs or post-synaptic terminals (red), and electrical junctions (green). Top: AVAL; Bottom: PVCR.

By examining the type of synapses near the soma of neurons with long projections and more than 25% of head/tail synapses near the cell body, (101 neurons), we find a small group of 12 neurons with predominately post-synaptic terminals (>75%) near the cell body (above red line in Figure 3.3C). With the exception of AVEL/R, all of these neurons are either outliers (AVAL/R, DVA,

PVCR) or very close to being outliers (AVBL/R, AVDL/R, AVL). Within this group, AVEL/R are the only neurons that do not have neurites spanning the entire length of the worm: their cell bodies are in the head and processes project halfway down the worm, terminating anterior to the vulva. The shorter span might be the reason why AVEL/R do not emerge as outliers.

The directionality of synapses (input or output) near the cell body is a structural property capable of identifying neurons important for integrative signalling in motor control. The collection of neurons with mostly inputs near the soma includes all, except PVCR, of the command interneurons (9 neurons) functionally identified as responsible for worm locomotion (Chalfie et al. 1985; Driscoll and Kaplan 1997). Wild type worms, when touched on the head, respond by moving backwards. Without AVA, AVD, and AVE, worms no longer exhibit this behavior. AVB and PVC are responsible for the exact opposite response: they mediate forward movement when worms are stimulated at the tail.

Although neurons in *C. elegans* appear isopotential and do not generate classical sodium ion (Na^+) action potentials (Goodman et al. 1998), command neurons may have special requirements to reach an activation threshold near the cell body before command signal can be passed along the process to distant targets. Physiological study will be necessary to understand the underlying mechanism for the position of pre- vs. post-synaptic terminals relative to the cell body.

The analysis of asymmetry in directionality of synapses revealed non-command neurons that appear to mediate motor functions. DVA, pre-synaptic to command interneurons and forward locomotion motor neurons, is involved in mechanosensory responses (Wicks and Rankin 1995). When subject to a diffused mechanical stimulus, such as a disturbance (e.g., tap) of the substrate on which the worm is resting, the worm responds by moving either forward or backward. Without DVA, the acceleration of such movement is diminished. AVL, acting in conjunction with neuron DVB, is critical for activating muscle contraction for defecation (McIntire et al. 1993a). RID has unknown function although both AVL and RID make neuromuscular connections to body muscles.

3.3.7 Wiring Optimization Using the Shared-Wire Model

To incorporate the importance of synapse location and directionality into theory, we propose an anatomically more accurate shared-wire model (Figure 3.1E, inset). In this model, each neuron is represented by a wire with multiple synapses. If a pair of neurons is synaptically connected, the corresponding wires must overlap. Similarly, if a neuron makes an external connection, the corresponding wire must include the location of that fixed point. Given these constraints, minimization of total wiring length (Weis and Mlynski 1987; Kennings and Markov 2000) yields the optimal placement of each synapse as well as the front and back ends of each neuron.

Since the actual locations of most synapses in the worm are not currently known, comparison with data requires predicting cell body positions. One possibility is to assign the cell body position to the center of mass of synaptic locations for each neuron. If connections are treated equally (analogous to the binary dedicated-wire model), the mean deviation of the predicted cell body location is 11.1% from actual. If connections are weighted by their multiplicity (number of synapses per connection analogous to the weighted dedicated-wire model), the mean deviation is 10.7%. In either case, the accuracy of the shared-wire model is no better than the dedicated-wire model.

However, the shared-wire model allows us to apply the results from outlier analysis by adopting different rules for the placement of cell bodies in neurons with specialized functions. First, we incorporate the observation that cell bodies of command interneurons gravitate towards post-synaptic terminals. For these neurons, the cell body is placed at the end of the neuron closest to the center of mass of post-synaptic terminals. Second, we incorporate the observation that cell bodies of neurons important in developmental pioneering are located on the opposite end of the neuron from the majority of synapses. For these neurons, we consider only the synapse-containing region (excluding connections to external structures). The cell body is placed at the end of this region most distant from the synaptic center of mass. Applying these rules for specialized neurons to the distribution of synapses obtained in the shared-wire model, we obtain a placement (Figure 3.1E and Shared-Wire

Model in Supplement) with mean deviation of 9.45%, better than predictions from the quadratic dedicated-wire model.

Wiring optimization using the shared-wire model makes an interesting prediction where a large fraction of all synapses congregates in a single anterior location along the worm (see Supplement, Figure 3.7 bottom). It is natural to associate this location with the nerve ring. Of course, as our model is one-dimensional, the actual three-dimensional structure of the nerve ring could not emerge. Yet, this congregation of synapses is an unexpected demonstration of the predictive power of wiring optimization.

3.4 Discussion

Here we showed that wiring minimization can establish a relationship between neuronal structure and function. We found that, for given connectivity, wiring optimization predicts the layout of many neurons in the animal despite some uncertainty about the exact form of the wiring cost. Thus, wiring optimization is a constructive approach for relating wiring diagram and neuron placement. Detailed comparison of the wiring optimization prediction and actual layout reveals neurons with special structural properties that have specialized function. Therefore, wiring optimization may also be used for predicting neuronal function.

Although wiring optimization establishes a structure-function relationship, there could be other factors affecting neuronal placement. In particular, we were unable to fully explain the placement and clustering of neurons belonging to the tail ganglia. In addition to the causes considered in the paper, other constraints could account for these discrepancies. For example, non-synaptic communication between neurons via neuromodulators or paracrine signalling is not accounted by wiring cost minimization. In principle, these constraints could be incorporated into the model if we knew which neurons participate in such signalling and what the cost-function is. Also, we ignored the volume exclusion effect which could push neurons away from their optimal positions (Chklovskii 2004b).

Finally, absence of clustering and relatively forward placement of the tail ganglia may be due to incomplete or ambiguous wiring data for posterior neurons (White et al. 1986).

Given that positions of neurons are optimized for specified functional constraints, what underlying biological mechanisms are responsible for such optimization in *C. elegans*? Experimental evidence suggests that wiring minimization may be driven by genetics as well as forces generated during embryonic and post-embryonic development. Studies that support evolutionary mechanisms show that the position of synapses can be perturbed without affecting cell body position and vice versa (Shen and Bargmann 2003). The identification of pioneers in the outlier analysis also demonstrates the importance of genetics in neuronal layout. Furthermore, a few neurons in the worm migrate long distances during development to positions where connection costs are lower than their initial positions (data not shown) (Hedgecock et al. 1987). However, mutant worms with miswired neurons demonstrate both wild-type as well as displaced cell body positions (White et al. 1992; Hamelin et al. 1993). This result and others suggest that neurites can exhibit tension *in vivo* (Condron and Zinn 1997) and *in vitro* (Bray 1979; Shefi et al. 2003). Such tension may pull connected cells closer together and optimize the layout during development (Van Essen 1997). We hope that future research will contribute to the field of evolutionary developmental biology by shedding light on the interplay between developmental mechanisms and genetic information in specifying neuronal position (Carroll 2005).

In conclusion, we showed that neuronal layout could be largely predicted by minimizing the wiring cost for given synaptic connectivity. The discrepancy between optimized and actual placement is mainly due to neurons with stereotypical roles in the network, such as developmental pioneers and command interneurons. This discrepancy may be due to the specialized requirements on the synapse placement relative to cell body. Although wiring optimization may not be the only factor in neuronal placement, it is the only one that has been quantified and has predictive power to relate neuronal structure and function.

3.5 Supplement

3.5.1 Connectivity Data

For the current work, we compiled an updated version of the *Caenorhabditis elegans* wiring diagram. Pivotal works published by (White et al. 1986)and (Hall and Russell 1991) had provided neuronal circuitry in the head and tail but lacked connection details for 58 motor neurons in the ventral cord of the worm. We compiled most of the missing data using original electron micrographs (EM) and handwritten notes from White and coworkers. The dorsal side of the worm around the midbody, however, was not previously documented. Using original thin worm sections prepared by White *et al*., we generated new EM images and reconstructed neurons with processes in this region (White et al. 1986). The new version of the wiring diagram incorporates original data and new reconstructions, as well as updates based upon later work (O. Hobert and D.H.H., unpublished work), and R. M. Durbin (http://elegans.swmed.edu/parts/neurodata.txt).

The wiring diagram of 279 nonpharyngeal neurons in *C. elegans* is now 97% complete, covering 6,393 chemical synapses, 890 electrical junctions, and 1,410 neuromuscular junctions. Over 3,000 connections, including chemical synapses, electrical junctions, and neuromuscular junctions, were added and/or updated from the previous version. Due to rather sparse sampling of data along lengths of the sublateral, canal-associated lateral, and midbody dorsal cords, connectivity ambiguities for a select few neurons remain.

The external connection cost consists of 200 sensory and motor neurons wired to 20 sensory organs, 95 body wall muscles, and one representative muscle for the vulva and anus, respectively. The identity of sensory neurons and the locations of their corresponding sensory organs are based on diagrams of amphids, phasmids, and putative touch sensors from the Wormatlas web site (www.wormatlas.org). A neuron is assumed to make a single connection to a given sensory organ.

The positions of muscles are used in two different ways in the paper, (*i*) location of external structures in optimization calculation (Eq. 3.3) and (*ii*) mapping of neuron-to-muscle connections for ventral cord motor neurons. For optimization, the position of each muscle is defined as the midpoint between anterior and posterior extremities of the sarcomere region (White et al. 1986; Dixon and Roy 2005). Neuron-to-muscle connections for the first 32 muscles in the head are detailed by (White et al. 1986). For the remaining muscles, direct neuron-to-muscle mapping is not available. In this case, we assume that motor neurons connect to muscles where positions of neuromuscular junctions overlap the sacromere region of a given muscle (Dixon and Roy 2005). Because more than one muscle can overlap the neuromuscular junction (NMJ) region of a single neuron, we approximate the number of connections to each muscle by taking the total number of NMJs made by a given neuron, divided by the number of muscles overlapping the NMJ region. For neurons lacking complete reconstruction, especially ones on the dorsal side of the worm, the number of neuron-to-muscle connections is assumed to be the average NMJ per muscle from fully reconstructed neurons of the same class. The last three body muscles in the tail of the worm do not overlap with NMJ regions. The connections to these muscles are assigned to the posterior-most motor neurons in the ventral and dorsal cords.

3.5.2 Neuron Position

We define neuron location by the center of the cell body projected onto the anterior–posterior (AP) axis of the worm. These positions are determined from various diagrams of neuronal cell bodies in the adult worm (www.wormatlas.org). We also divided neurons into three regions in the worm body: head, midbody, and tail. Head neurons have cell bodies located <25% along the AP axis from the head of the worm. Midbody neurons are located between 25% and 75% down the worm body from the head. Tail neurons are >75% down the worm body from the head.

3.5.3 Synapse Position

Despite the near completion of the wiring diagram, which maps connections between neurons, there is a lack of data specifying the location of individual synapses in the worm. Using neuron diagrams in (White et al. 1986), information from handwritten notes designating the source animal of the reconstruction (N2U vs. N2Y and JSE), and crossreferences with (Hall and Russell 1991), we approximated synapse positions into three gross categories: head (<25% of body length from the nose), midbody (between 25% and 75%), and tail (>75%). This data set was created by looking at individual neurons by themselves. Positions of synapses across pairs of neurons are not reconciled into these gross categories. A synapse is considered to be in proximity of the cell body if both fall within the same defined areas of head, midbody, or tail.

3.5.4 Ganglia Distribution

The positions of neurons within each ganglion are more dispersed in the wiring cost minimization placement than the actual layout, especially for the three posterior-most ganglia. Fig. 3.5 shows the mean deviation and corresponding standard deviations between predicted and actual positions of neurons in each ganglion. The largest dispersion of deviations is attributed to neurons belonging to the preanal, dorsorectal and lumbar ganglia.

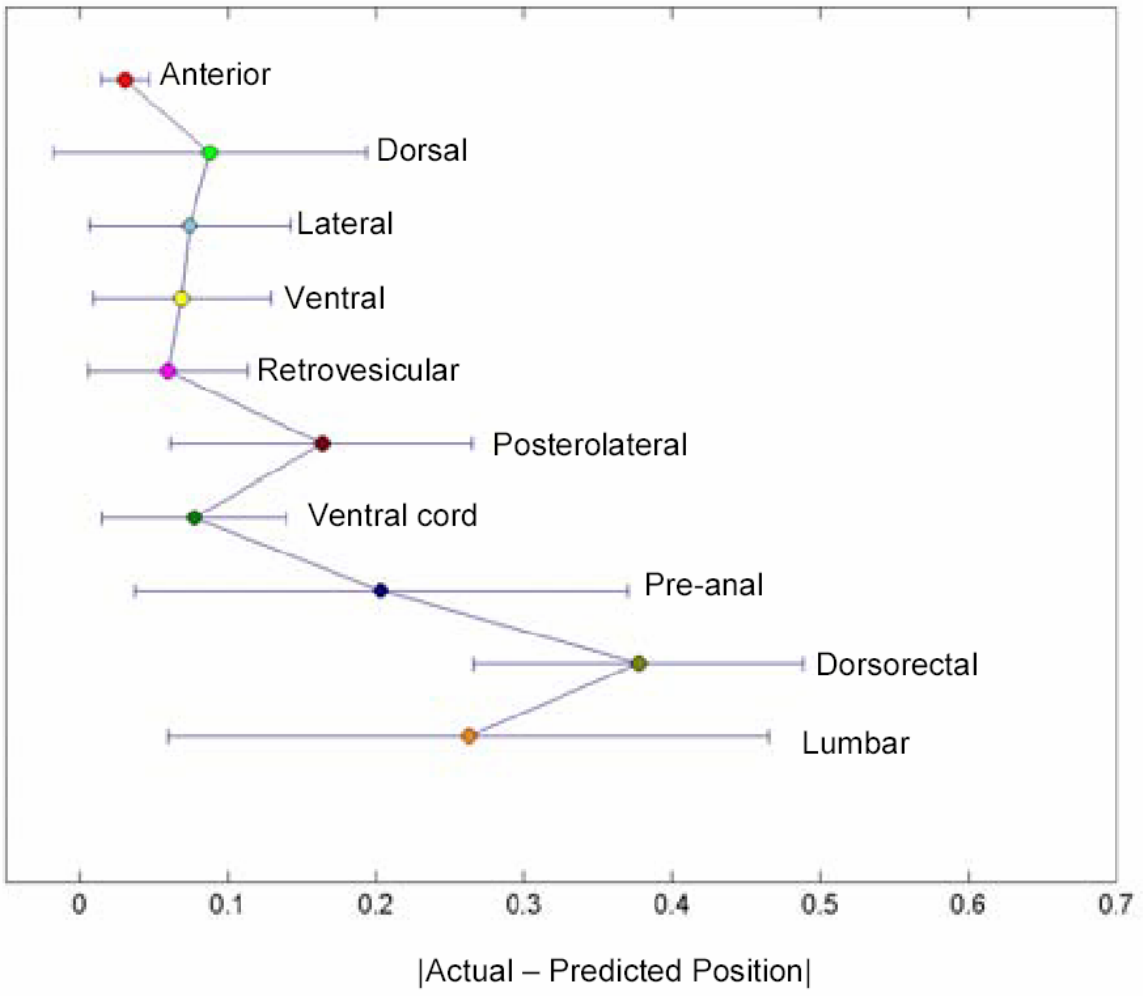

Figure 3.5: Predictability of positions of neurons belonging to the same ganglion from wiring minimization. Each dot represents the mean positional deviation from actual of neurons within the given ganglion. Error bar shows the first standard deviation from the mean.

3.5.5 General Power-Law Cost Function

To test the robustness of the cost minimization results, we explored several alternative forms of the cost function where cost is proportional to different powers of wire length. Mathematically, we replaced the exponent, ζ , in Eqs. 3.2 and 3.3 with values between 1 and 4. Unlike the quadratic formulation, power-law cost functions with exponents $\neq 2$ are not exactly solvable. However, if the exponent is greater than one, these cost functions are convex (Sigl et al. 1991), meaning that any local minimum must be global as well, thus simplifying the minimization task.

We minimized these cost functions by using several effective numerical techniques. First, we used the conjugate gradient method, which converges particularly well for exponents greater than about 1.5. Second, we used an iteration procedure based on the quadratic cost function (Sigl et al. 1991). This technique converges particularly well when the exponent is below 3. Third, we used linear programming to solve the case of exponent equal to one by introducing additional variables (Weis and Mlynski 1987). For those exponents where cost functions can be solved by different methods, we verified that the corresponding solutions coincide.

Fig.3.6A shows the mean deviation between predicted and actual neuron position as a function of α and ζ . To understand the dependence of layout on these parameters, we show the "trajectories" of neuron locations for different α with $\zeta = 2$ (Fig. 3.6B). In the limiting case of large α, neurons with sensory endings are located close to the fixed points. In the limiting case of small α , neurons bunch up unrealistically close to each other. Best agreement between predicted and actual is achieved at intermediate values of α . The fit gets worse for smaller α , because neurons from lumbar ganglion move too far forward and for larger α , because neurons in the nerve ring ganglia move too far backward

A

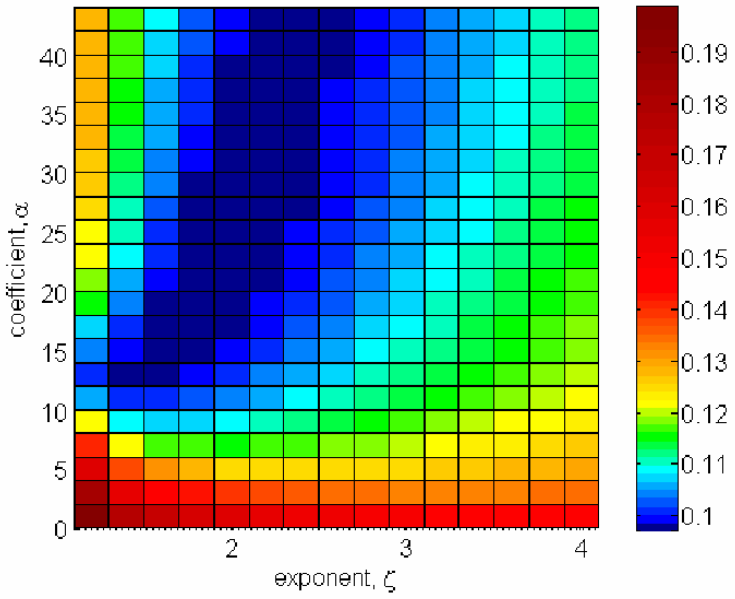

B

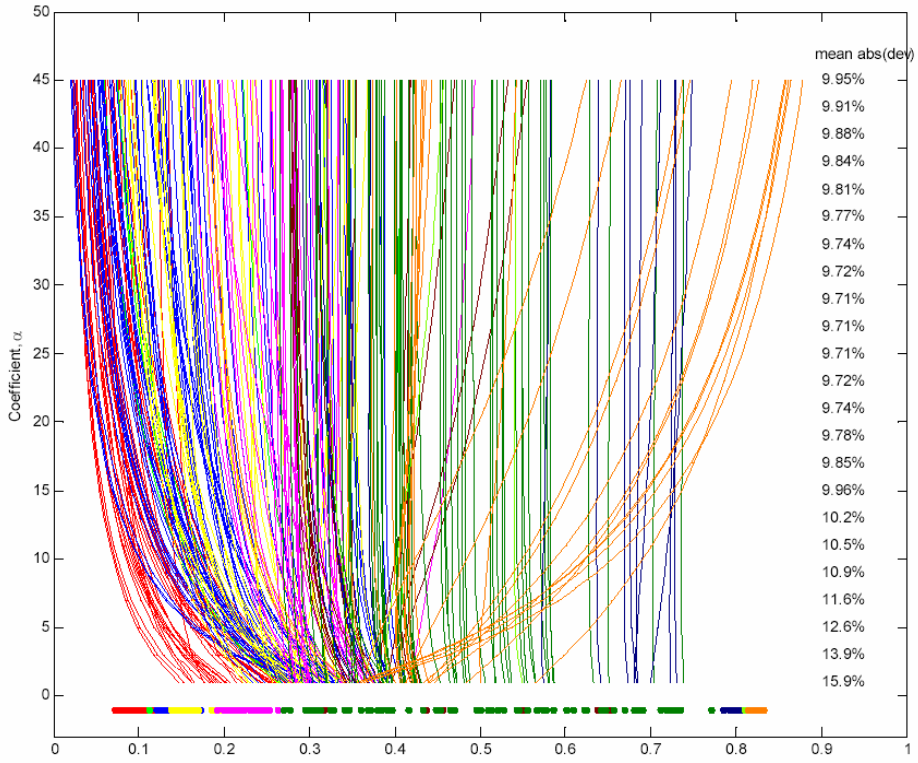

Figure 3.6. **A.** Mean of the absolute value of predicted–actual position for different values of the normalization coefficient (α) and the wire length power (ζ). Interestingly, the minimum average deviation is achieved by the quadratic cost function with $\alpha = 27$, close to biologically justifiable 29.3. **B.** Neuron positions for different values of normalization coefficient, α , at $\zeta = 2$. Colors indicate which ganglia neurons belong to, according to the code of Fig. 3.1. For the sake of clarity only unpaired or left neurons are shown.

3.5.6 Shared-Wire Model

In this formulation, each neuron is represented as a single straight wire with multiple synapses on it (Fig. 3.1E *Inset*). Wires belonging to synaptically coupled neurons must overlap. Then the cost function is the sum of each neuron's wire length. By introducing variables corresponding to the front and back tips of each wire, this cost function can be solved by linear programming (Weis and Mlynski 1987). In addition to the tips of wires, the solution yields locations of synapses (Fig. 3.7). When two synaptically coupled neurons had an extensive overlap region, we placed the synapse between them at the midpoint of that region. Because the actual locations of most synapses in the worm are not currently known, comparison with the data requires predicting cell body positions (see above, *Neuron Position*). The center of mass of synapses for each neuron was used as the position of its cell body. Multiplicity of connections may be included in this model by weighting synapses correspondingly.

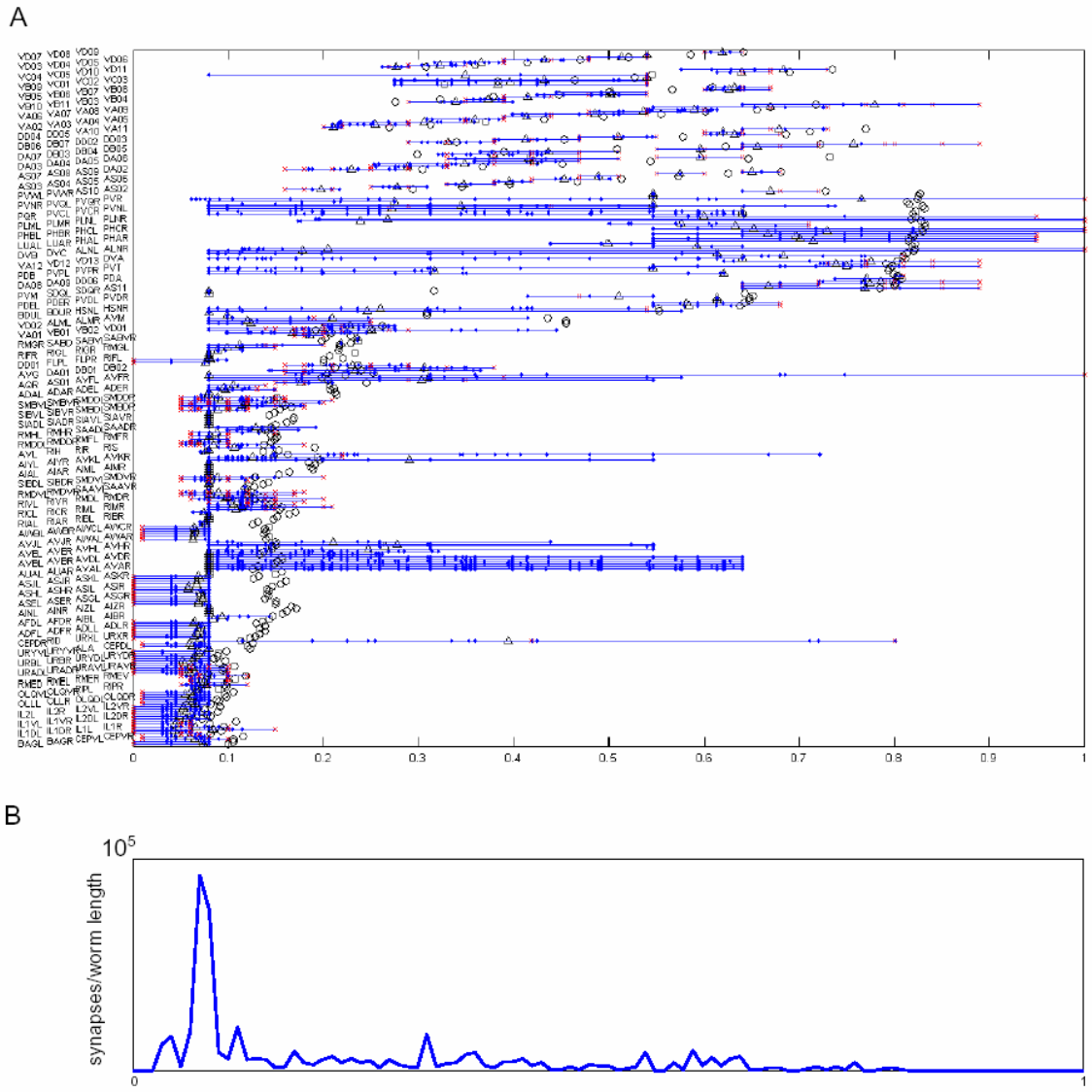

Figure 3.7: A. Optimal synaptic and neuronal layout in the shared-wire model. Neurons are vertically offset for clarity. Each neuron is shown by a blue line with cell body position indicated by a black triangle. Synapses are blue dots and fixed points are red crosses. A circle indicates actual cell body position. **B.** Predicted distribution of synaptic density in the shared wire model. Unexpectedly, a peak in synaptic density emerges in the anterior region, which corresponds to the nerve ring. This result demonstrates predictive power of the wiring optimization approach.

3.5.7 Lineage Analysis

We constructed a matrix of "relatedness" between neurons expressed in terms of distances using published embryonic and postembryonic lineage trees (Sulston 1976; Sulston et al. 1983). "Relatedness" between two neurons is found by first identifying the lowest common progenitor cell. Then, for each cell, we count the number of cell divisions from the common ancestor where each division is defined as a single unit in length. The lineage distance is the total number of cell divisions from the two neurons with the initial division from the common progenitor counted only once. Two hundred seventy-nine nonpharyngeal neurons are included in the analysis. Postembryonic blast cells are mapped back to the embryonic lineage such that all cells can be traced to the anterior daughter of the fertilized egg P0. In cases where variability has been noted in the left-right pair of postembryonic cells, we assigned the precursors to what is most often observed in experiment (Sulston and Horvitz 1977). Specifically, blast cell P1 is assigned to the right and P2 is assigned to the left. Cells that appear to be random in left/right division have been arbitrarily assigned such that P3, P5, P7, and P9 are right, and P4, P6, P8, and P10 are left. AVFR has been assumed to come from P1.aaa and AVFL from W.aaa. Ambiguities of postembryonic P cells affect mostly ventral cord motor neurons.

Because cell divisions split lineage trees into left/right or AP branches, optimization results, not surprisingly, show distinct left and right neurons clusters (data not shown). This effect gives rise to large deviation between predicted and actual placement of neurons, because bilateral neurons are usually located near each other along the AP axis in the animal. We test the sensitivity of left/right lineage to layout prediction by calculating the solution for unpaired and left neurons only (186 neurons). This methodology improves the mean deviation slightly (24.5% compared with 26.1% for all 279 neurons) but is still a worse prediction than the wire-minimized solution based on neuron connectivity.

3.5.8 Data Files and Notes

Data used in the paper are available from the authors at http://www.wormatlas.org/handbook/nshandbook.htm/nswiring.htm.

Footnote

[*] Results of this work were presented at the 2004 Computational & Systems Neuroscience (CoSyN) at Cold Spring Harbor Laboratory, New York.

Acknowledgements

We are very grateful to John White and Jonathan Hodgkin for donating archival EM data from MRC/LMB to the Center for *C. elegans* Anatomy. We thank Michael Hengartner who pointed out the attractiveness of *C. elegans* as a model organism, and Carlos Brody, Josh Dubnau, Yuri Mishchenko, Alex Koulakov, Catharine Rankin and Markus Reigl for helpful discussions. BLC is the recipient of an Arnold and Mabel Beckman Graduate Student Fellowship of the Watson School of Biological Sciences. DC is supported by NIMH grant number 69838 and Klingenstein Foundation Award. The Center for *C. elegans* Anatomy is supported by NIH RR 12596 to DHH.

Chapter 4: How do worms move?

4.1 Introduction

The simplicity of *C. elegans* physiology has prompted various groups to study the relationship between behavior and the neuronal network. One of the most stereotyped behaviors of the worm is forward and backward locomotion. Much like a snake, worm movement consists of sinusoidal undulations. To progress forward, worm propagates a backward traveling wave from the head to the tail. Conversely, a forward traveling wave propagates from posterior to anterior of the body for backward motion. Using Newtonian mechanics, several studies (Gray 1953) for snakes and (Erdös and Niebur 1990; Niebur and Erdös 1991) for worm) derived equations of motion to describe how muscles along the body must contract to generate sinusoidal undulations necessary for propulsion. Using a simplified version of the neuronal network, Niebur and Erdös calculated whether signals generated by synchronous neuronal excitation can predict the speed of locomotion (Niebur and Erdös 1993a; Niebur and Erdös 1993b). Although the model produced undulations, the calculated neural activity in *C. elegans* was two orders of magnitude faster than observed velocity of the body wave. This discrepancy could be due to the reliance on command interneurons to support the wave or attributed to the incompleteness of the wiring diagram used, and, at the time, the lack of electrical properties for *C. elegans* neurons.

Several studies also approached the problem from the opposite direction: using behavior as the starting point to model neuronal network. Ferrée and Lockery constructed a linear network to simulate chemotaxis, nematode response in the presence of attractive/repulsive chemicals (Ferrée and Lockery 2001). Similarly, Wicks used the tap response behavior to predict polarity of connections between sensory and inter-neurons (Wicks et al. 1996). These studies contributed to the understanding of select functional components of the neuronal circuit. Nevertheless, without information at the motor neuron and muscle level, detailed descriptions of worm behavior remained elusive.

With the availability of the full wiring diagram (Chapter 2), we will explore the fundamental properties of the *C. elegans* motor network and compare the result to actual worm locomotion. This chapter is divided into two parts: Section 4.2 is a study of worm locomotion using calcium imaging of body wall muscles of moving, behaving worms. The results will be compared to experiments and theoretical predictions made in other model systems. Section 4.3 describes a linear model derived from the connectivity diagram and its ability to predict observed worm locomotion.

4.2 Calcium imaging

4.2.1 Introduction

As described earlier, *C. elegans* generates sinusoidal undulations to move forward and backwards. However, the properties of the waveform, such as amplitude, frequency, and speed of the wave can vary dramatically depending on the physical environment. For example, when placed on a hydrated agarose pad versus in liquid, the waveform of movement can be quite different (Fig. 4.1). These differences in locomotion may be the result of different neural programs, the forces imposed by the environment, or a combination of both. From simple observation of worms in the laboratory, one cannot distinguish between locomotive forces exerted by the muscles and reactionary elastic and frictional forces.

In order to build the model of neuronal movement control, we need to know the pattern of muscle activity required for locomotion. Body wall muscles in *C. elegans* receive simultaneous excitatory acetylcholine and inhibitory γ-aminobutyric acid (GABA) inputs from motor neurons (Lewis et al. 1980; McIntire et al. 1993a; McIntire et al. 1993b; Richmond and Jorgensen 1999). Upon depolarization, muscle cells experience an influx of extracellular calcium ions (Ca^{2+}) through voltage-gated calcium channels as well as Ca^{2+} stored in the sarcoplasmic reticulum (Maryon et al. 1998; Jospin et al. 2002). The free calcium binds to troponin-C, activating the contraction apparatus of the sarcomere (Alberts et al. 2002). The resulting tension is transferred to the worm body through

lateral attachments distributed along the entire length of the cell (Francis and Waterston 1985). Previous imaging experiments have shown that the magnitude of calcium transients in the cell correspond to the amplitude of inward Ca^{2+} current (Jospin et al. 2002). In this study, we looked directly at worm-generated forces by imaging calcium transients in body wall muscles during locomotion.

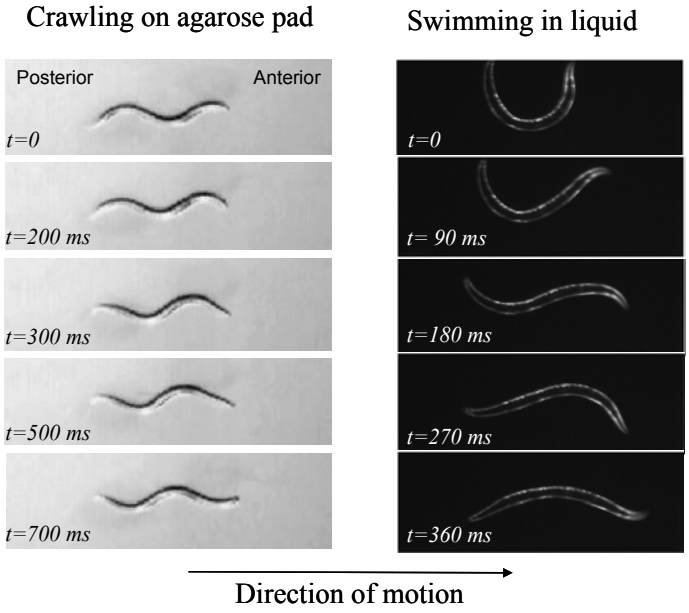

Figure 4.1: Worm undulation waveforms on agarose pad versus in liquid. Direction of motion is from left to right.

To detect changes in calcium concentration in muscle cells of moving worms, we used a ratiometric calcium indicator, yellow cameleon 2 (YC2) (Miyawaki et al. 1997). Several detailed studies have shown cameleon to be a viable indicator of *C. elegans* neuron and muscle activity (Kerr et al. 2000; Shyn et al. 2003; Suzuki et al. 2003). However, no published work thus far has been conducted on freely moving animals. The cameleon molecule consists of a calcium-binding calmodulin protein (Xenopus XCaM) with a calmodulin binding protein M13, flanked by a cyan fluorescent protein (CFP) on one end and a yellow fluorescent protein (YFP) on the opposite end (Fig.

4.2). Calmodulin with empty calcium binding sites is a dumbbell-shaped molecule. This conformation separates the two fluorescent proteins on opposite ends of the cameleon from interacting efficiently with each other. Therefore, excitation at cyan wavelength produces mostly CFP emitted light, giving a low YFP/CFP ratio. However, in high Ca^{2+} concentrations, calcium-bound calmodulin becomes compact and binds to M13, shortening the distance between CFP and YFP.

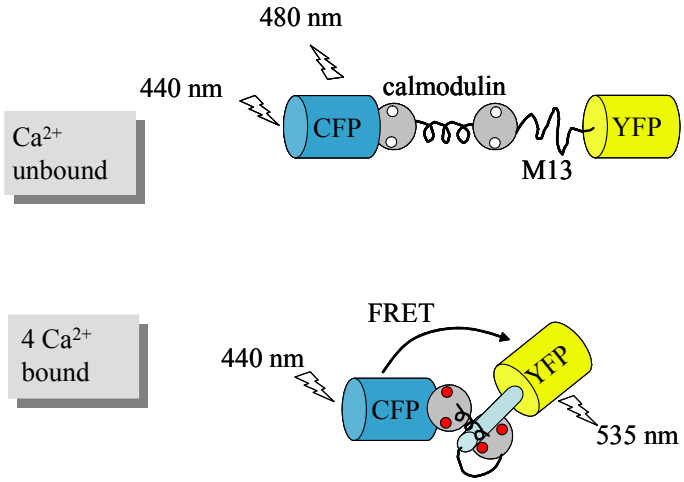

Figure 4.2: Yellow cameleon molecule with and without calcium bound. Adapted from (Miyawaki et al. 1997).

Under these conditions, cameleon excited with cyan light would emit mostly at YFP wavelengths due to fluorescence resonance energy transfer (FRET), resulting in an increase in YFP/CFP. This effect is reversible upon unbinding of Ca^{2+} from calmodulin. The ratiometric sensor is also well suited for detecting calcium transients in behaving animals because changes in intensity of each fluorescent protein from motion artifacts automatically cancel each other in the ratio.

In this section, we used calcium imaging to investigate the patterns of muscle activity as worms moved forward and backward. We also explored limits of worm muscle activity by partially restraining worm body movements. To determine how the worm propels itself, we correlated the force exerted by individual muscles to the local body curvature. A spatial distribution of force was then determined by comparing muscles activity versus curvature over time.

Since the worm body stretches as it bends around a curve, we studied the effect of muscle activity to the amount of stretch. In the 1980's, Russell (*unpublished*) proposed that long, sparsely-connected processes of motor neurons may function as "stretch receptors". Since then, researchers have found a putative mechanosensory channel expressed along the processes of a subset of motor neurons (Tavernarakis et al. 1997). However, direct evidence of stretch reception in these neurons has not been observed. To investigate this question, we correlated individual muscle activity with the amount of stretching anterior or posterior to the muscle position during both forward and backward locomotion.

4.2.2 Results

4.2.2.1 Visualization of Muscle Activity in Freely Moving Worms

To image calcium transients in muscles of moving worms, we used a line of worms, *kyEx302*, which expressed extra-chromosomal arrays of YC2 (yellow cameleon 2) under the *C. elegans myo-3* promoter specific to body wall, vulva, and enteric muscles (Okkema et al. 1993). The worms displayed mosaic fluorescence with 50-75% of body wall muscle expressing cameleon. Vulva muscles had 100% expression and were typically the brightest cells in the body. Worm body muscles are oblong-shaped cells along the anterior-posterior axis with tapered ends. In adult animals, each muscle is approximately 100μm in length and 1.5-4μm in diameter at its broadest point. Fluorescence appeared uniform inside each cell with occasional punctuate spots. Due to the mosaic nature of the cameleon worms, the most anterior and posterior foci of a single muscle cell could sometimes be identified. Rows of body wall muscles are organized into four quadrants: two ventral and two dorsal rows. In our experimental setup, the worm moves in a two-dimensional plane where it lies on its side and makes dorsal-ventral bends. As a result, the left and right muscle quadrants are indistinguishable from each other. Figure 4.3 shows an unprocessed fluorescence image of both CFP and YFP channels

with typical cameleon expression. Depending on the imaging session, we would focus on either the left or right rows of ventral/dorsal muscles.

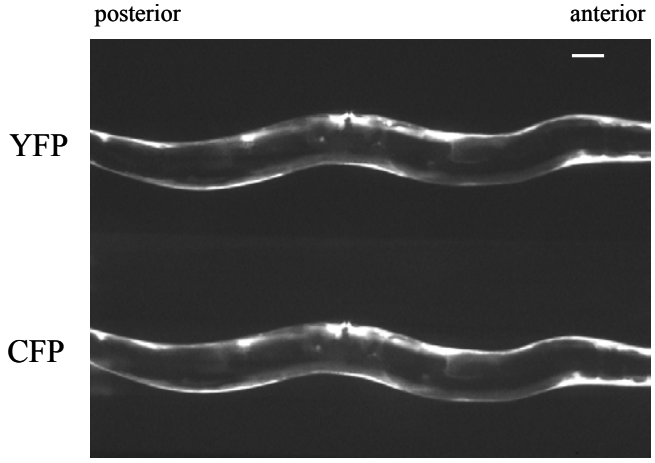

Figure 4.3: Typical unprocessed fluorescent image from microscope camera. Top image is YFP, bottom is CFP. Scale bar: 50 μm.

Calcium movies of freely moving and partially restrained worms were recorded. We studied muscle activity of worms in several different environments: on semi-rigid two-dimensional substrate (6% hydrated agarose pad), in liquid droplet or in a liquid-filled device with either a large chamber (an area where worms can freely move) or a long, thin channel (diameter approximately 1 to 2 times the thickest part of the worm body). Worms displayed typical crawling motion (>1.5 wavelengths per body length, <1 Hz in frequency) on the agarose pad and in liquid-filled channels and typical swimming motion in liquid droplet or liquid-filled chambers (0.5-1.5 wavelengths per body, 1-2 Hz in frequency).

Figure 4.4 shows frames from a movie of a typical forward crawling or swimming worm in a liquid-filled channel. The color and hue saturation of the images denote the pixel-by-pixel ratio of YFP to CFP intensities, scaled between 0.6 and 1.1. The variation in color represents the change in calcium concentration in the cell. To highlight cameleon expressing cells in the mosaic animal, we set the brightness of the images by the averaged intensity of YFP and CFP signals. As the worm moved through one cycle of undulation, calcium transients in muscle cells also oscillated through one cycle of high and low concentration. This effect was especially prominent in the two ventral muscles flanking the vulva and the dorsal muscle near the neck of the worm (denoted by arrows). Fluorescence emission appears to be elevated (muscle becomes the reddest) just prior to reaching the greatest bend (concave away from muscle cells) as denoted by *.

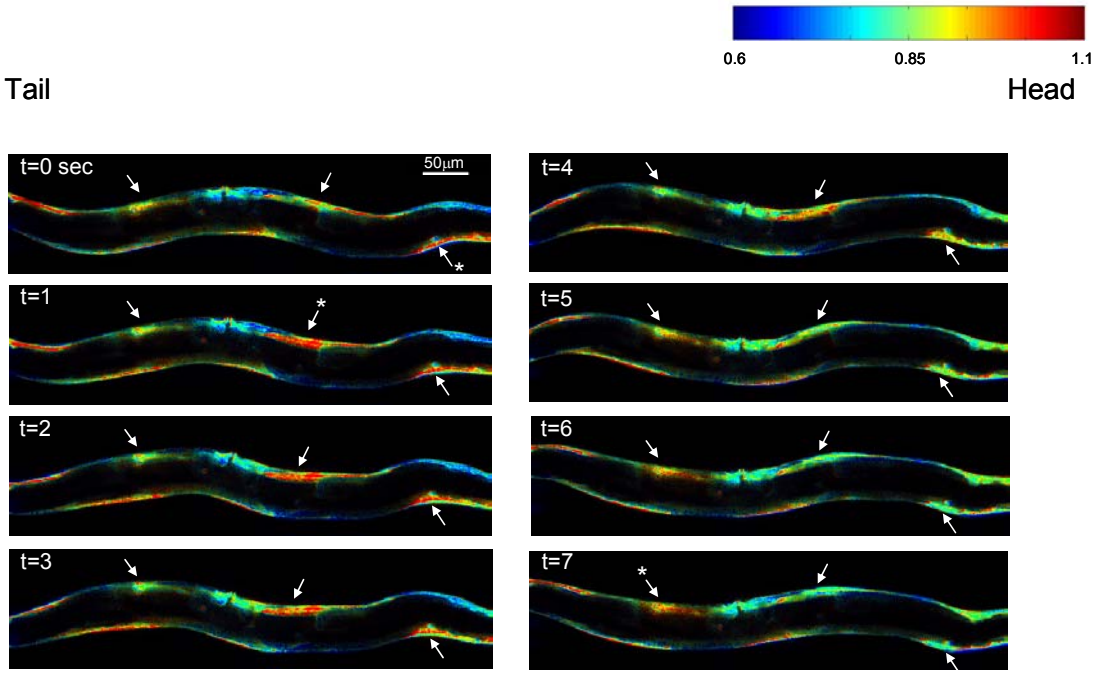

Figure 4.4: Movie of a typical forward crawling or swimming worm in a liquid-filled channel. The color and hue saturation of the images denotes the pixel-by-pixel ratio of YFP to CFP intensities, scaled between 0.6 and 1.1, scale bar denotes 50 μm.

To track activity of muscles along the worm body over time, we extracted rows of ventral and dorsal muscles from each frame of the movie and aligned the muscle positions in time (see Methods Section **4.2.5.3**). In Figure 4.5, typical patterns of muscle activity for a forward-crawling worm are shown for 5 cycles over 30 seconds. The horizontal axis denotes positions along the worm body in micrometers; the vertical axis shows time in seconds; and color represents amount of calcium transients (YFP/CFP fluorescence). A muscle cell in this young adult worm is approximately 63 μm along the horizontal axis. As the worm crawls forward, waves of muscle activity travel from head to tail (denoted by arrows). Conversely, in backwards moving worms (for both swimming and crawling), we observed muscle waves traveling from tail to head (data not shown). Therefore, waves of muscle activity are consistent with the direction of locomotion: backward traveling wave during forward locomotion and forward traveling wave for backward movement.

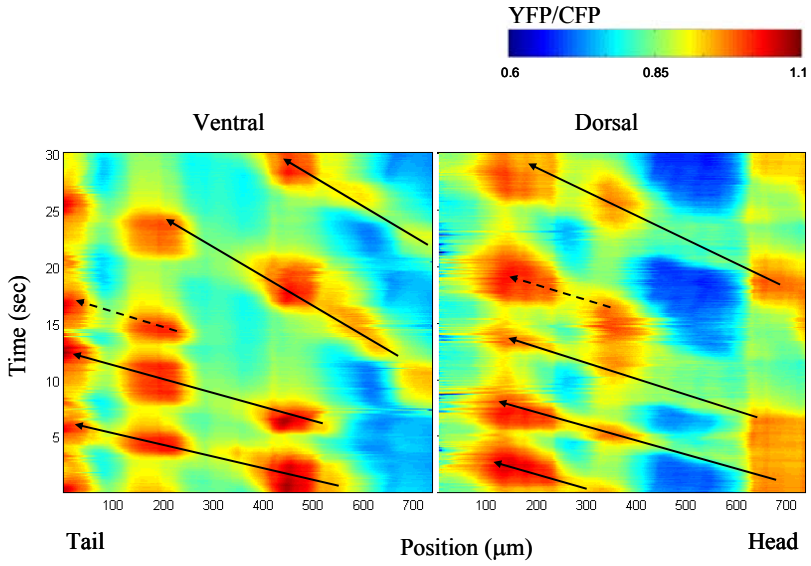

Figure 4.5: Typical ventral and dorsal muscle activity patterns for a forward-crawling worm. Arrows show waves of muscle waves traveling from head to tail (dashed arrows indicate waves that initiated mid-body). Color represents YFP/CFP scaled between 0.6 and 1.1. Vulva is located near position 300. Length of one muscle cell: 63 μm.

Interestingly, we found that muscle waves did not always originate from the extreme ends of the worm (dashed arrows in Fig. 4.5). In Figure 4.6, two cycles of anterior-traveling muscle waves originate from a position anterior to the vulva. Muscles posterior to this position were unconstrained and had been observed to move with appropriate changes in calcium transients (data not shown). However, we must note that the tail of the worm in Fig. 4.6, just off the field of view of the microscope, was restrained in a thin channel. Perhaps the position of wave initiation was related to this confinement.

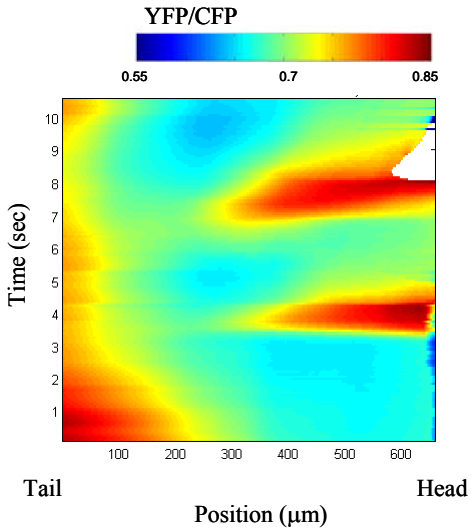

Figure 4.6: Waves initiating in mid-body. Large adult worm with two cycles of anterior-traveling muscle waves start from a position anterior to the vulva (position 100). Color denotes YFP/CFP scaled between 0.55 and 0.85. Length of one muscle cell: 200 μm. Worm tail out of field of view was restrained.

Dorsal and ventral muscle patterns in Figures 4.5 appear by eye to be out of phase: elevated ventral activity is opposed by reduced dorsal activity. We quantify this offset by finding the correlation between the activity of opposing ventral and dorsal muscles. Figure 4.7 gives two examples of correlations for forward and backward moving worms. Although correlation function can vary for different muscles, no clear patterns emerged between forward vs. backward moving worms or anterior vs. posterior muscles. We found the average correlation to be -0.73±0.18 for 9 muscles across 3 animals.

To verify that our observations are indeed the result of calcium changes in muscle cells, we tested three lines of calcium-insensitive cameleon worms (*kyEx1250, kyEx1251,* and *kyEx1252*). These control animals expressed a mutated version of cameleon where all calcium binding sites had been disrupted, therefore, insensitive to Ca^{2+} (Starovasnik et al. 1992). Imaging results showed no evidence of muscle waves for both forward and backward crawling control worms.

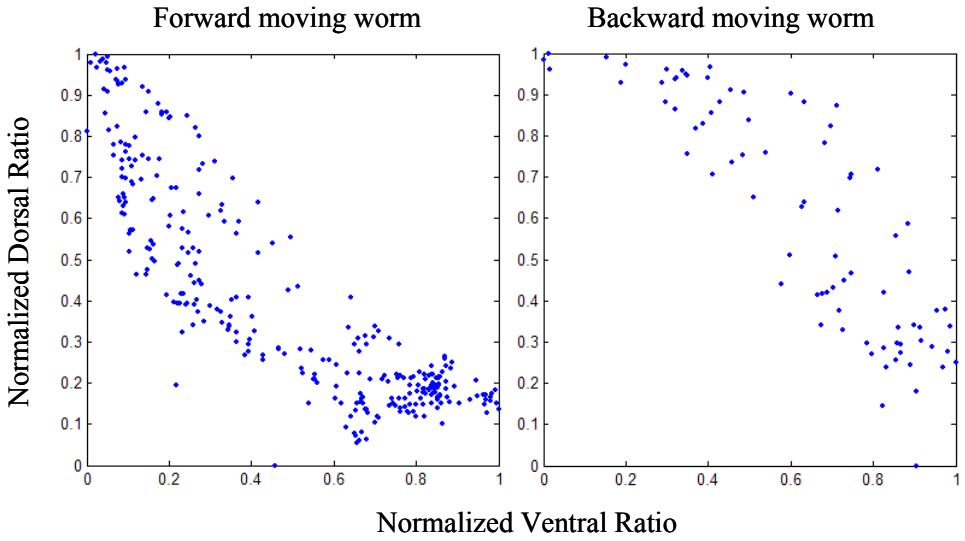

Figure 4.7: Correlations of dorsal-ventral muscle activity. Activity of a dorsal muscle is plotted as a function of the activity of its opposing ventral muscle over multiple cycles of undulation. Muscle activity is represented by normalized YFP/CFP ratio (scaled between maximum and minimum ratio for the given muscle and time period).

4.2.2.2 Instantaneous Muscle Activity Relating to Body Bend and Stretch

To gain understanding of the propulsive forces underlying worm movement, we studied the distribution of muscle activity along the worm as a function of body curvature. Experiments combining calcium imaging and electrophysiological recordings have shown that muscle cell depolarization leads to calcium current influx and increased levels of intracellular Ca^{2+} (Jospin et al. 2002). The activity of worm muscles is related to this calcium transient (Kerr et al. 2000). To quantify net change in calcium concentration, or instantaneous muscle activity, we calculated the change of YFP/CFP ratio over time (time-derivative of the ratio). We assume that this instantaneous

muscle activity is related to force exerted by the muscle. In our analyses, positive curvature denotes concave bend towards ventral side while negative curvature refers to the amount of bend towards the dorsal side (Fig 4.8A). When the body is straight, curvature is zero. Assuming that muscle length is directly related to curvature (see section 4.2.6.4), dorsal muscle would be the longest at positive curvatures and ventral muscle longest at negative curvatures.

Figure 4.8B shows phase diagrams of ratio change versus body curvature for muscles of a forward crawling animal, arrow indicates direction in time. Influx of Ca^{2+} in ventral muscles starts just before the body reaches minimum curvature, with the greatest influx at or after this bend. Calcium level starts to decrease (negative influx) just prior to maximum curvature (numbers 1, 2, and 3, respectively in top panel of Fig. 4.8B). The reverse is seen on the dorsal side (bottom panel of Fig 4.8B). As show in diagrams of Fig. 4.8C, the region of Ca^{2+} influx appears to shift slightly towards smaller curvatures (left of the graph) for posterior muscles.

We test the hypothesis of stretch sensors by correlating Ca^{2+} influx, and thus muscle depolarization, with the length of nearby muscles. For forward moving worms, we found correlation between rate of ratio change and stretching of posterior muscles (Figure 4.9). The same activity was found to have no correlation with the length of anterior muscles. The comparison was made between muscles separated by a distance of two cell lengths. For backward crawling worms, muscle contraction rate is positively correlated with the stretch of anterior muscles and no correlation with the stretch index of posterior muscles (data not shown). These results were seen in all muscles along the worm body.

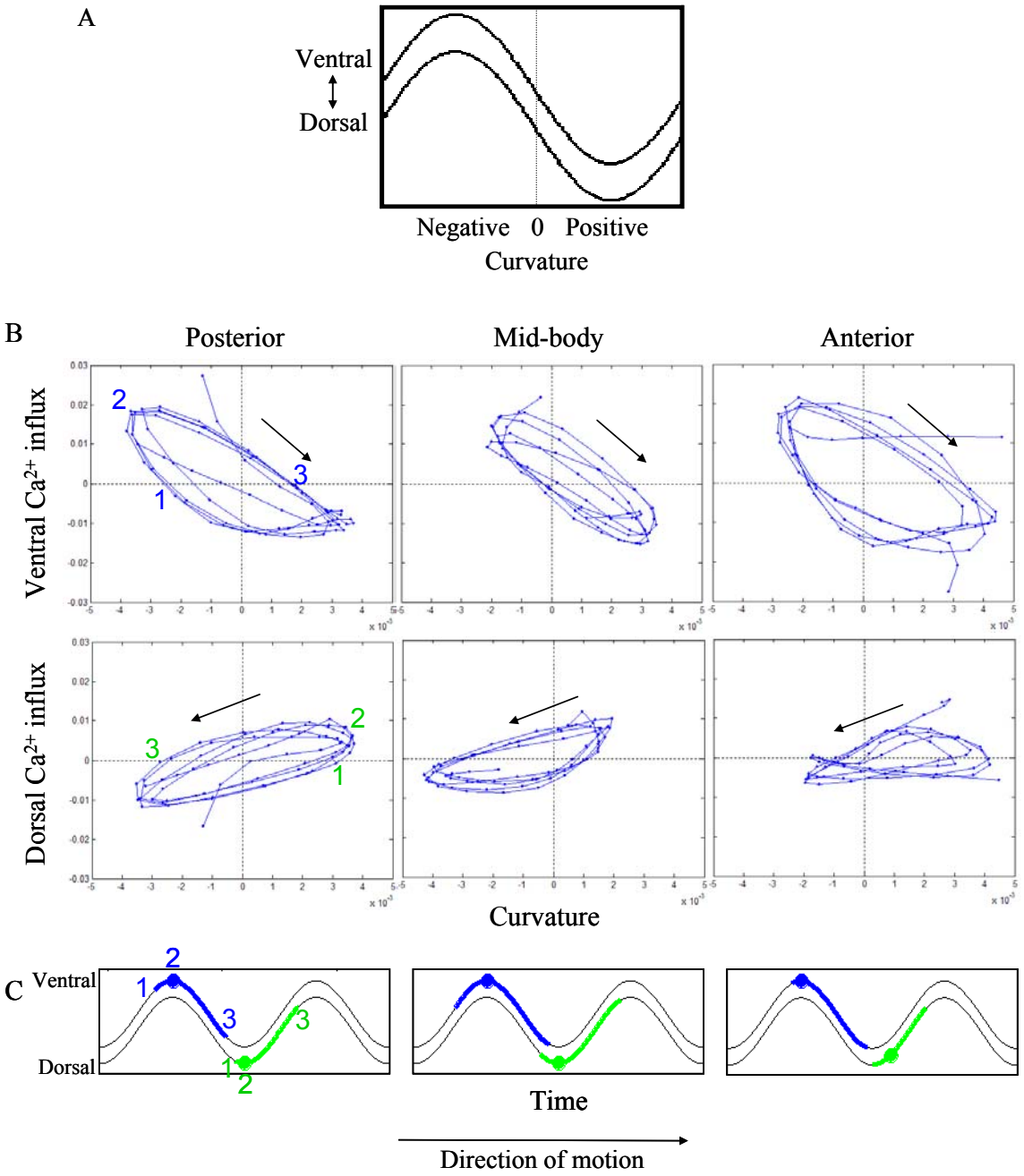

Figure 4.8. **A.** Worm body posture at different curvatures. **B.** Phase diagrams of Ca^{2+} change versus body curvature for muscles along the body of a forward crawling animal, arrow indicates direction in time. Calcium change is represented by time-derivative of YFP/CFP ratio. Numbers in the left panels show (1) Start of Ca^{2+} influx; (2) Position of maximum Ca^{2+} influx; (3) End of positive Ca^{2+} influx. Top row: ventral muscles; Bottom row: dorsal muscles. **C.** Cartoon depicting positions of Ca^{2+} influx relative to curvature for ventral (blue) and dorsal (green) muscles in one cycle of movement. Horizontal axis indicates time. Dots show position of maximum Ca^{2+} influx (position #2 in B).

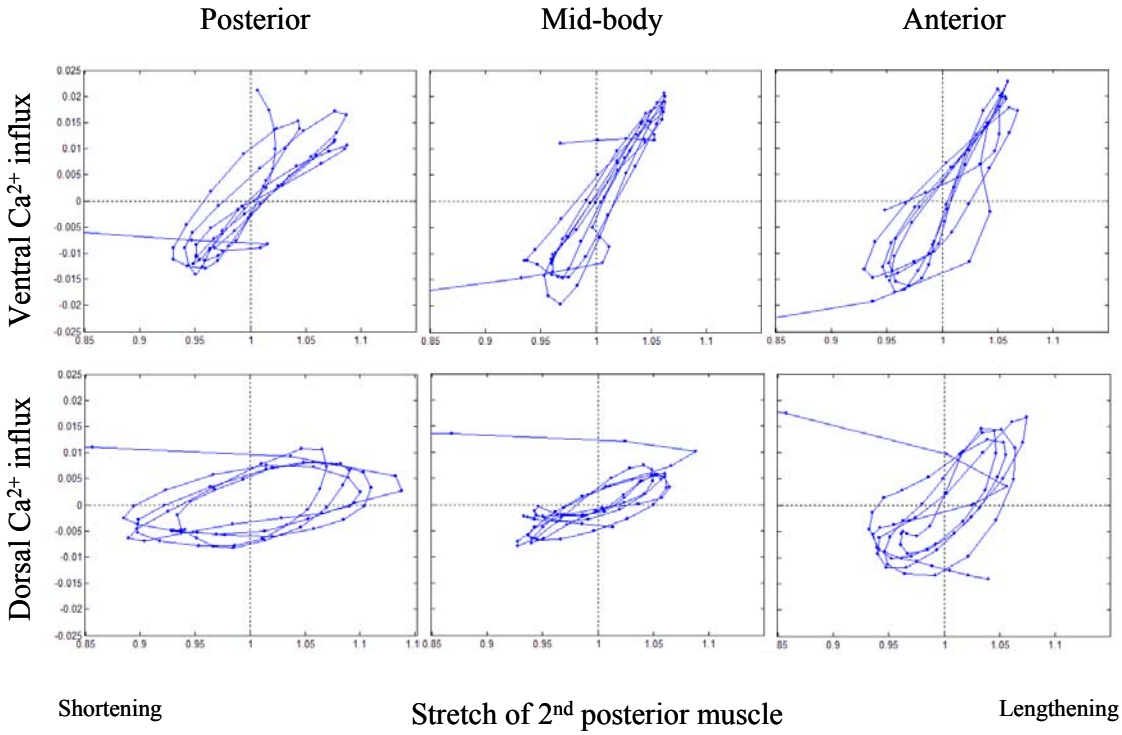

Figure 4.9: Correlation of Ca^{2+} influx in muscle cells with stretch of a posterior muscle two cell lengths away. Data is from a forward moving worm. Ca^{2+} change is represented by time-derivative of YFP/CFP ratio. Stretch is defined by the difference in length of a body segment in an active worm versus a completely relaxed worm (lengthening: stretch > 1; shortening: stretch < 1).

4.2.2.3 Muscle Waves in Partially Immobilized Worms

The limits of muscle wave propagation were explored through a series of studies where the worm body was partially immobilized. In these experiments, the worm was imaged in a liquid-filled device where a portion of the body (head, tail, or mid-body) was trapped in a 40 μm constriction (Figure 4.10A). We found that when worms were restrained at mid-body, muscle waves on the two sides of the constriction always traveled in the same direction, but often at different frequencies and phases (7 movies between 3 animals). Figure 4.10B shows the muscle patterns for a representative worm in such a configuration. In the first 10 seconds of the movie, we observed three cycles of oscillation along the posterior portion of the worm versus just one cycle in the anterior portion. When the worm changed direction of motion (at time = 15 sec), muscle waves on both the anterior and posterior portions of the body reversed directions simultaneously. Occasionally, we did observe complete passage of muscles waves through the constriction along the entire length of the worm body (arrow in Fig. 4.10B). For animals immobilized at the head or tail through constriction in a thin, straight channel, muscle waves would start or end at the boundary between the restrained and freely moving parts of the worm. No change in calcium transients were ever observed in the restrained portions of the worm (data not shown).

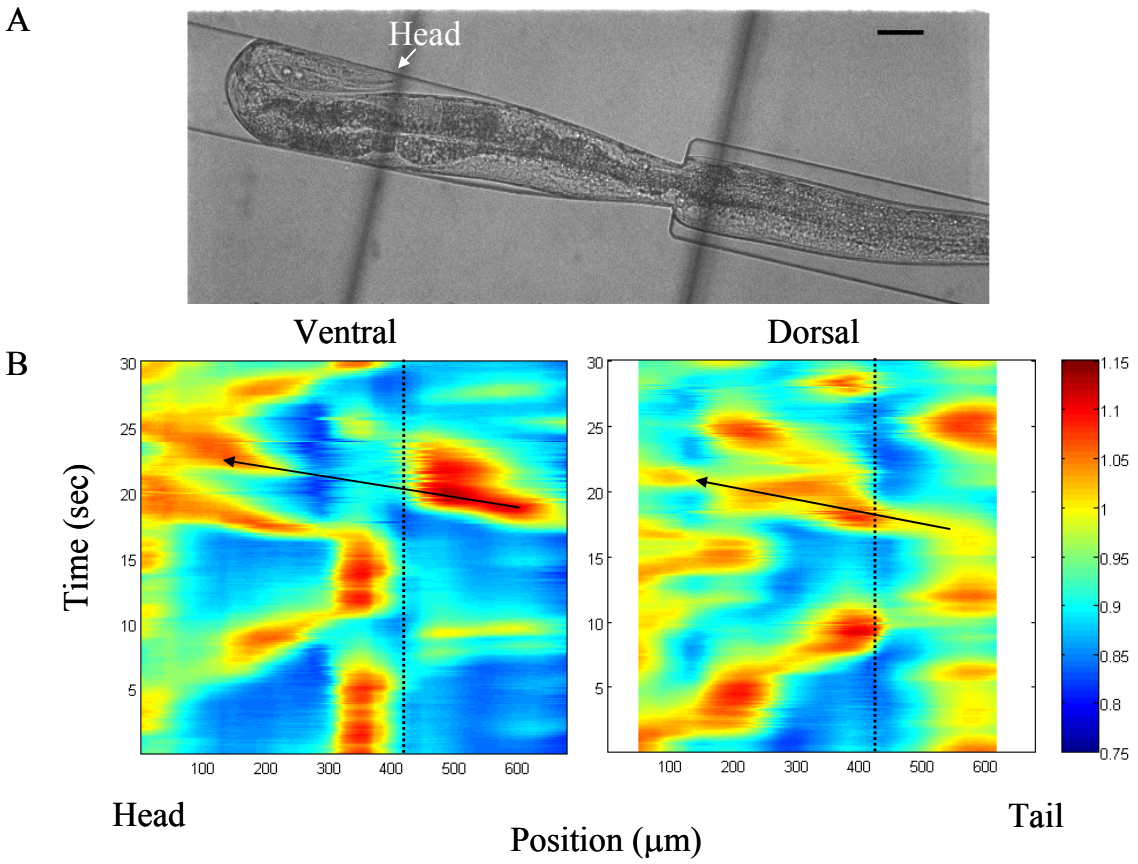

Figure 4.10: **A.** A worm with mid-body constricted in a 40 μm opening. Head is bent on itself on the upper left of the channel. Scale bar: 50 μm. **B.** Muscle patterns of an immobilized worm constricted at mid-body. Dashed line marks the position of constriction. Arrows show a wave propagating through the constriction. Worm switches from forward to backward motion at time = 15 seconds. Color denotes YFP/CFP scaled between 0.75 and 1.15.

4.2.3 Discussion

Our imaging experiments have demonstrated the detection of calcium transients in muscle cells of freely moving and partially restrained worms. For the first time, we are able to directly ascertain propulsive forces generated by the worm without having to disentangle the array of complex environmental forces imposed on the animal.

4.2.3.1 Muscle Activity Correlates with Body Shape in a Stereotypical Manner

The pattern of muscle activity is consistent with worm locomotion. Forward movement is characterized by backward-traveling body and muscle waves and backward motion by forward-traveling waves. In addition, we found calcium transients in muscles correlate with the shape of the worm body in a stereotypical manner. The onset of muscle activity always precedes maximum curvature. These results are independent of undulation direction and waveform, such as amplitude, frequency, and speed, which varied up to a factor of two for worms moving in different test environments. The above evidence demonstrates that the worm plays an active role in creating its posture rather than passively allowing external forces to shape its body.

The activity of ventral-dorsal muscles is found to be phase-shifted by approximately 180 degrees. This coordination between opposing ventral-dorsal muscles supports the widely regarded cross-inhibition model where muscle contraction on the two sides of the worm are exactly out of phase. From genetics and neuron ablation experiments, classes of excitatory cholinergic and inhibitory GABAergic motor neurons have been identified in adult worms (Lewis et al. 1980; McIntire et al. 1993a; McIntire et al. 1993b; Jin et al. 1999). Electron micrograph reconstructions show the excitatory neurons on the ventral side to be simultaneously pre-synaptic to ventral muscles as well as opposing dorsal GABA neurons, vice-versa is true for dorsal side excitatory neurons (White

et al. 1986). The net result of this model is the inhibition of muscles on one side when the opposing side is active, as verified by calcium imaging of ventral-dorsal muscles.

4.2.3.2 Spatial Distribution of Muscle Activity

By correlating the rate of YFP/CFP ratio change to local body curvature, we showed evidence that calcium starts to flow into muscle cells prior to reaching maximum body bend. A number of published works (Gray 1953; Gray and Lissmann 1964; Wallace 1968; Erdös and Niebur 1990; Niebur and Erdös 1991; Niebur and Erdös 1993a; Niebur and Erdös 1993b) examined locomotion generated by sinusoidal undulations in snakes and nematodes. These studies suggested that, to create propulsive force, muscles are active when approaching a region of increasing curvature. For example, in forward motion, the muscle beneath a concave up curve becomes active before it reaches maximum bend (Fig. 7 in (Gray 1953)). Our results are qualitatively consistent with these theories.

However, a closer look at the distribution of instantaneous muscle activity as a function of curvature revealed disagreements between imaging results and previous models. Gray predicted that muscle is active as bending increases from curving towards the muscle to away from the muscle with the largest activity located at zero curvature (Fig. 7 in (Gray 1953)). Using a stretch receptor model, Niebur *et al.* showed muscle activity for increasing curvatures from where body is bent towards the muscle and zero curvature (Fig. 3 in (Niebur and Erdös 1993a)). Our imaging data demonstrated both types of patterns with spatial distribution dependent on the muscle position (anterior, mid-body, or posterior) where the peak Ca^{2+} influx is near the region where the body bends towards the muscle. Shifting of muscle activity as a function of muscle location relative to the anterior-posterior axis of the animal was previously seen in electrical recordings of lamprey muscles during swimming (Williams 1989). This study found the effect to be the result of muscle waves traveling faster than the mechanical wave. A more detailed study of *C. elegans* locomotive dynamics would be required to see if the same mechanism applies in worms.

4.2.3.3 Evidence for Stretch Receptors

By correlating local changes in worm body length with nearby muscle activity, we found evidence consistent with the proposed direction of stretch receptors. Studies have shown *C. elegans* to have dedicated motor neurons for forward versus backward movement (Chalfie et al. 1985). These distinctly asymmetric neurons are mirror images of each other in structure: forward neurons have long, sparsely-connected processes extending towards the tail while backward neurons' long processes project toward the head of the worm (White et al. 1976; White et al. 1986). Russell hypothesized that these long processes contain "stretch receptors" which allow the motor neuron to sense local body shape (*unpublished*). The expression of putative mechanosensory channels (*unc-8* and *del-1*) have since been found in these neurons (Tavernarakis et al. 1997). Our imaging data demonstrated elevated muscle activity when the worm body is stretched in the directions described above for forward and backward motion. Although our results support the presence of proposed proprio-sensory receptors, experiments that directly probe the activity of motor neurons as a function of local body stretch are still needed.

4.2.3.4 Limits of Muscle Waves Provide Clue to Neural Mechanism

The series of interesting observations from our imaging study of partially immobilized worms offer clues to the underlying neural mechanisms of locomotion. First, we found that the entire worm always moved in the same direction, either forward or backward, regardless of the position of restraint on the worm body. *C. elegans* possess a set of inter-neurons that are specifically responsible for forward or backward motion (Chalfie et al. 1985). Our result is consistent with the idea of a "command" signal that dictates the direction of movement. However, we also observed that worm body on either side of a constriction can move with different frequencies. Perhaps the "command" signals do not communicate undulation frequency nor participate in the coordination of wave

propagation. In regions of the worm body where it was straight and completely immobilized, no changes in calcium transients were detected. This finding suggests that local bending might be necessary for the initiation and propagation of muscle waves. The partially-restrained worm experiments demonstrated some examples in the limits of muscle wave dynamics. A more in-depth study of muscle activity with incrementally controlled restraints supplemented by mutants with known wave propagation defects would be necessary to substantiate our observations.

4.2.4 Conclusion

In conclusion, calcium imaging of muscles in moving worms has allowed us to visualize worm-directed activity in freely moving and partially restrained worms. We described stereotypical patterns of muscle activity during forward and backward locomotion. Using imaging results, the relationship between worm propulsive forces and body shape were compared with theoretical models and observations in other animals. Finally, experiments using partially restrained worms provided clues to the underlying neural mechanism for motion control. In the next section, we will use the worm motor neural network derived from Chapter 2 to model the observed patterns of muscle activity.

4.2.5 Experimental Methods

All experiments, including worm rearing, molecular biology, and optical imaging, were performed in Cori Bargmann's laboratory at Rockefeller University with generous assistance by Manuel Zimmer as well as other members of the Bargmann lab.

4.2.5.1 Plasmids and Worm Strains

Worms were grown at room temperature on standard nematode growth medium (NGM) seeded with *E. coli* strain OP50 as a food source.

Cameleon *myo-3*::YC2 plasmid and expression of the plasmid in worms containing extrachromosomal arrays (*kyEx302*) were made by Jami Dantzker from Cori Bargmann's laboratory at University of California, San Francisco. The worms displayed mosaic fluorescence in body-wall and vulva muscles with 50-75% of tissue specific cells expressing cameleon. Fluorescence appeared uniform in each cell with occasional punctuate spots.

Calcium-insensitive cameleon worms were constructed by changing the position 12 glutamic acid (E) to glutamine (Q) at each of the four calcium binding sites (E31Q, E67Q, E104Q, and E140Q) on the calmodulin sequence of the *myo-3*::YC2 plasmid (Starovasnik et al. 1992). Using the *Pfu* polymerase methodology provided by QuikChange kit (Stratagene), we performed site-directed mutagenesis of the first nucleic acid of glutamic acid from guanine (G) to cytosine (C) using the following primers (A: adenine, T: thymine, G: guanine, C: cytosine): Binding site #1: 3' GGC ACC ATC ACC ACA AAG CAA CTT GGC ACC GTT ATG 5'; Binding site #2: 3' GGA ACG ATT TAC TTT CCT CAA TTT CTT ACT ATG ATG GCT AG 5'; Binding site #3: 3' CGG CTA CAT CAG CGC TGC TCA ATT ACG TCA CG 5'; Binding site #4: 3' GGC CAA GTA AAC TAT GAA CAG TTT GTA CAA ATG ATG ACA GC 5'. The resulting construct (50 μg/ml) was injected into N2 worms. Three lines with uniform expression in body-wall muscles were isolated and designated *kyEx1250, kyEx1251, kyEx1252*.

4.2.5.2 Imaging

Worm imaging was performed on a Zeiss Axioskop 2 upright microscope with a 10X Zeiss air objective. Excitation light was provided by a Mercury lamp at 100 W power passing through a 440nm (40nm bandwidth) dichroic filter. A 1.0 neutral density filter was sometimes used to attenuate the light source. Emitted light passes through a commercially purchased beam splitter, Dual-View MicroImager made by Optical Insights. The splitter contains a dichroic filter which splits the light into two paths. One path is filtered by a cyan emission filter (480nm, 40nm bandwidth) while the

other by a yellow emission filter (535nm, 30nm bandwidth). The two light paths are projected simultaneously onto a Photometrics CoolSNAP$_{HQ}$ 1392 x 1040 pixels (6.45 x 6.45 μm^2 pixel size) CCD camera. The data was collected on a PC using MetaMorph version 6.3r2 (Universal Imaging) and each movie frame saved as individual TIFF files.

4.2.4.3 Worm preparation and recording

One-day-old hermaphrodite adults and L4 worms were used for imaging. Worms were imaged under two different conditions. In the first method, 6% agarose pads were used as the worm locomotion medium. A drop of M9 solution was dripped onto the pad just prior to the transfer of a single worm from the cultivation plate. The worm was immediately placed under the microscope for imaging as it swam in the drop of M9. Approximately 3 minutes later, the liquid would be mostly absorbed by the agarose pad, leaving behind a slippery film of agarose/M9 mixture. At this time, the worm's movement resembled crawling with typical crawling waveforms and frequency. However, due to the slippery film at the top of the agarose pad, the worm slips with each undulation and stays within the field of view of the microscope. Fluorescence movies were obtained under these conditions and marked as "crawling" worms. In some imaging sessions, worms were placed directly onto the slippery film such that crawl locomotion would be imaged without the worm transitioning from swim to crawl.

In the second imaging preparation, a microfluidic worm chip made of polydimethy-siloxane (PDMS, a transparent material with elastic properties similar to rubber) was used to house the worm. The design, fabrication, and methodology for use of the device were developed by Nikolas Chronis of the Bargmann Lab (now at University of Michigan). Figure 4.11 shows the geometry of the 1 cm x 1 cm worm chip used: an open region leads to a thin channel 900 μm length x 70 μm width x 28 μm depth, both filled with either S. Basal buffer solution (no cholesterol) or M9. A single worm would be transferred to the device by first picking it to an unseeded plate using a platinum wire and covering it

with a drop of liquid (buffer or M9). Then, some of the liquid along with the worm was sucked into a thin Teflon tube connected to the device and flushed into the open region of the chip through fluid pressure changes. In the open region of the device, a L4 worm would move freely as if in a drop of liquid on agarose. Older and fatter worms would be confined by the depth of the device and would move more in a crawling fashion (1.5-2.5 wavelengths per body length, < 1 Hz in frequency). In the thin channel, L4 and older worm would always "crawl" with fatter worms containing more wavelengths per body length than thinner worms. Although the worm would clearly pass multiple cycles of sinusoidal bends through its body, it would make very little forward or backward progress due to slippage. This effect kept the worm in the field of view of the microscope for the duration of a typical 300 frame movie with 60-100 millisecond exposure per frame and 2 x 2 binning (the speed of the camera-to-computer interface limited the maximum frame rate to around 16 frames per second at 2 x 2 binning). Worms were imaged individually with an average of 5 movies collected from each worm.

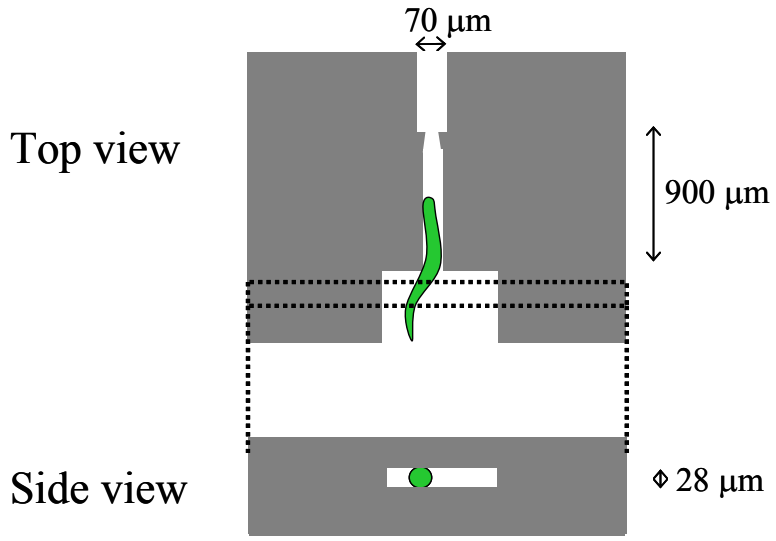

Figure 4.11: Diagrams of top and side views of worm device used during imaging. Drawing is not to scale. Green object represents the worm, gray regions denotes PDMS, and open regions is filled with buffer or M9.

4.2.6 Image Analysis

Data obtained from fluorescent imaging were analyzed using software modules written in MATLAB 6.5 (MathWorks Inc.). Changes in calcium transients are indicated by changes in the ratio of YFP to CFP signals. Below I describe image processing steps used to quantify calcium transients in body wall muscle cells.

4.2.6.1 Alignment

As mentioned previously, the yellow (CFP) and cyan (YFP) filtered light channels were projected simultaneously onto the microscope camera and saved as a single image by the computer. The two channels must be in good register with each other in order to obtain proper ratio of YFP to CFP. Throughout each imaging session, reference images of each worm were taken using transmitted white light. These images were used for alignment and for verifying position of the worm inside the worm chip. For some imaging sessions, only fluorescent images were available as reference. The same alignment procedure was applied to both types of images.

Each reference image was split into two with one containing YFP signal and the other CFP signal. Well-focused features in the images were chosen by eye and manually clicked in as paired reference points for alignment (30 – 200 points). Cross-correlation of the paired points was then applied to hone in on the true location of the reference points. Using the aggregate of the new paired points, alignment of the two channels was calculated using a 2^{nd}-order polynomial spatial transformation. Depending on the drift of the imaging system, an alignment transform was calculated approximately once for every three movies.

4.2.6.2 Ratiometric Movie and Background Signal

Using the calculated alignment transform, each worm movie was, pixel-by-pixel, converted into an YFP/CFP ratiometric movie. As before, each frame in the movie was first split into

individual YFP and CFP images and aligned using previously obtained alignment transform. Then, a background signal for each channel was obtained and uniformly subtracted.

A background signal for each channel was obtained by first calculating the histogram of intensities for the entire image. This histogram included both background and calcium-related intensities. By looking through histograms for all frames in the movie, we determined the frequency contribution of calcium changes to intensity bins of the histogram. This value was used to set a new minimum frequency in all intensity bins, effectively shifting the original histogram downwards uniformly in frequency (y-axis). The new histogram was fitted with a Gaussian distribution and the peaked used as the backward signal.

4.2.6.3 Fluorescence from Muscle Cells

To quantify the activity of muscles related to locomotion, we needed to isolate muscle cells from the imaged worms and compare the calcium transients of each muscle during worm locomotion. Using MATLAB's image analysis toolbox, an outline of the worm with thickness equivalent to the width of muscle cells (10 – 30 pixels) was drawn. The outlined worm was then split lengthwise into ventral and dorsal sides. This outline was used as a mask for rows of ventral and dorsal muscles. The YFP and CFP fluorescence of each muscle cell were calculated by taking the sum of intensities in an area defined by the width of the outline and length of 60 – 200 pixels, depending on the size of the worm. Since the anterior and posterior points of each muscle cell could not always be identified, the intensity of each muscle was taken as a running sum along the length of the worm body.

As the worm moved forwards and backwards during imaging, the position of a given muscle would change position in each frame of the movie. To track worm movement, we used the vulva muscle as a landmark. The coordinates of either the anterior or posterior vulva muscle was manually clicked into the computer on each frame. The positions of muscle cells were approximated by the Eucleidian distance anterior or posterior to the vulva.

However, as the worm bends during movement, its body stretches around the outside portion of a convex curve and shortens on the inside portion of the same curve. Therefore, the vulva muscle as a landmark alone was not sufficient for determining the positions of lengthening and shortening muscle cells. To account for this effect, we used an unconstrained nonlinear optimization algorithm in MATLAB to refine the positions obtained from vulva landmark. Rows of ventral (or dorsal) muscles from each movie frame were aligned to a reference frame using the averaged fluorescence of YFP and CFP channels. The algorithm maximized the correlation between the frame in question and the reference frame using the following transform:

$$x' = x + s(1)\sin(kx) + s(2)\cos(kx) + s(3)\sin(2kx) + s(4)\cos(2kx) \qquad (4.1)$$

where x' is the transformed position, x is the initial position, s is a vector containing the optimization variables, and k was empirically set to 0.005. With positions of muscles properly aligned from frame-to-frame, we could easily extract the calcium signals from each cell over time.

4.2.6.4 Local Body Stretch and Curvature

As mentioned above, the worm body stretches and shortens locally as it bends around a curve. The muscle alignment from stretch compensation, in effect, provided information regarding the amount of stretch at each position along the worm body. To obtain "stretch", we first found the positions of muscles for a completely relaxed worm (no stretching or contraction) by taking the average muscle alignment transform over 3-4 full cycles of movement. Since the body experienced both lengthening and shortening in a complete cycle, this average provided the positions of the muscles along the worm body at rest. The amount of stretching and contraction was then given by the change in relative positions of muscles in the active worm versus the relaxed worm.

The degree of stretching in the body is correlated but not equivalent to body curvature. To find curvature, we calculated the first and second spatial derivatives of the outlined worm along the anterior-posterior axis for each movie frame and used the standard definition for curvature:

$$curvature = \frac{\frac{d^2 l}{dx^2}}{\left(1+\left(\frac{dl}{dx}\right)^2\right)^{\frac{3}{2}}} \tag{4.2}$$

where l is the outline of the worm and x is the position along the anterior-posterior axis.

4.3 Linear Model of Worm Locomotion

4.3.1 Introduction

In the previous section, we described the efforts worms make during forward and backward movement through calcium imaging of muscle activity. But what controls the muscles? *C. elegans* muscles receive synaptic inputs from motor neurons and are electrically connected to neighboring muscles via gap junctions (White et al. 1986). Electrophysiological recordings of muscles have shown that the gap junctions mediate coupling between adjacent left-right cells but not between adjacent anterior-posterior cells (Liu et al. 2006). Therefore, the propagation of muscle waves must be coordinated by the neural network.

In leech and lamprey, where components of the motor network can be easily probed and recorded, the neural control of sinusoidal undulations has been extensively studied and modeled (Lockery and Sejnowski 1993; Marder and Calabrese 1996; Grillner et al. 1998; Cacciatore et al. 2000; Zheng et al. 2007). In *C. elegans*, on the other hand, stimulation and measurement of neuronal activity in an intact, behaving motor system have proved cumbersome and difficult. Direct assay of the neuronal network (single or multiple neurons) in freely moving worms has never been accomplished. As a result, most theoretical models of locomotion have been based on behavioral and genetic studies, limited to the level of directional or turning control of worm movement (Zhao et al. 2003; Dunn et al. 2004; Sakata and Shingai 2004; Pierce-Shimomura et al. 2005). Only a few studies have tackled the details of how the worm body undulates during locomotion, either using Newtonian mechanics (Gray and Lissmann 1964; Karbowski et al. 2006), or neuronal modeling (Niebur and

Erdös 1993a; Bryden 2003). Unfortunately, without the full wiring diagram of the nervous system, previous theoretical models have omitted several key characteristics of the mid-body motor network. In this section, we will model the patterns of muscle activity observed during locomotion using a linear model derived from the actual connectivity diagram of the motor system.

Motor neurons controlling *C. elegans* body muscles fall into seven classes (more control neurons in the head) (White et al. 1976; White et al. 1986). Forward locomotion is specifically controlled by a set of dorsal (DB) and ventral (VB) neurons while another set of dedicated dorsal (DA) and ventral (VA) neurons are responsible for backward motion (Chalfie et al. 1985). These directionally-defined neurons are excitatory onto body muscles (Lewis et al. 1980) and have distinctly asymmetric morphology along the anterior-posterior axis: forward neurons have long, sparsely-connected processes extending towards the tail while backward neurons' long processes project toward the head of the worm (Figure 4.12) (White et al. 1976). As we mentioned earlier, these long processes have been hypothesized to contain "stretch receptors" which allow the motor neuron to sense local body shape (Russell, *unpublished*). All four classes of neurons receive input signals on the ventral side from command inter-neurons located in the head or tail of the animal (AVB/PVC for forward motion and AVA/AVD for backward motion) (Chalfie et al. 1985). Another class of neurons on the dorsal side (AS) is similar in connectivity and structure to DA neurons without the extended processes. Therefore, they have typically been regarded as backward motor neurons (Altun and Hall 2002-2006). The remaining two classes of motor neurons, located on the dorsal (DD) and ventral (VD) side, are not directionally specific in function or morphology. These neurons are GABAergic and inhibitory on body wall muscles (McIntire et al. 1993a; McIntire et al. 1993b; Richmond and Jorgensen 1999). Instead of receiving inputs from inter-neurons, the DD/VD neurons are post-synaptic to excitatory motor neurons on the opposite side of the worm: DD receives inputs from VA and VB, VD from DA/AS and DB. This pattern of connectivity has been dubbed "cross-inhibitory" because the excitatory motor neurons are simultaneously pre-synaptic to same-side muscles and

opposite-side inhibitory neurons. The net effect is excited muscles on the ventral side and inhibited muscles on the dorsal side or vice versa.

To complete the wiring diagram we infer the neuron-to-muscle connectivity using the following consideration (also see Section 3.5.1). In *C. elegans*, body muscles send processes to the nerve bundle in order to make synaptic connections with motor neurons instead of vice versa (White et al. 1986; Hedgecock et al. 1987; Dixon and Roy 2005). During EM reconstruction of the nervous system, the origins of these muscle "arms" were not followed for cells behind the pharynx. Therefore, the target muscles of motor neurons in the body were not identified. However, since mid-body muscle arms are localized within their sarcomere regions (Dixon and Roy 2005), we used the positions of neuromuscular junctions to approximate which motor neurons connect to which muscles.

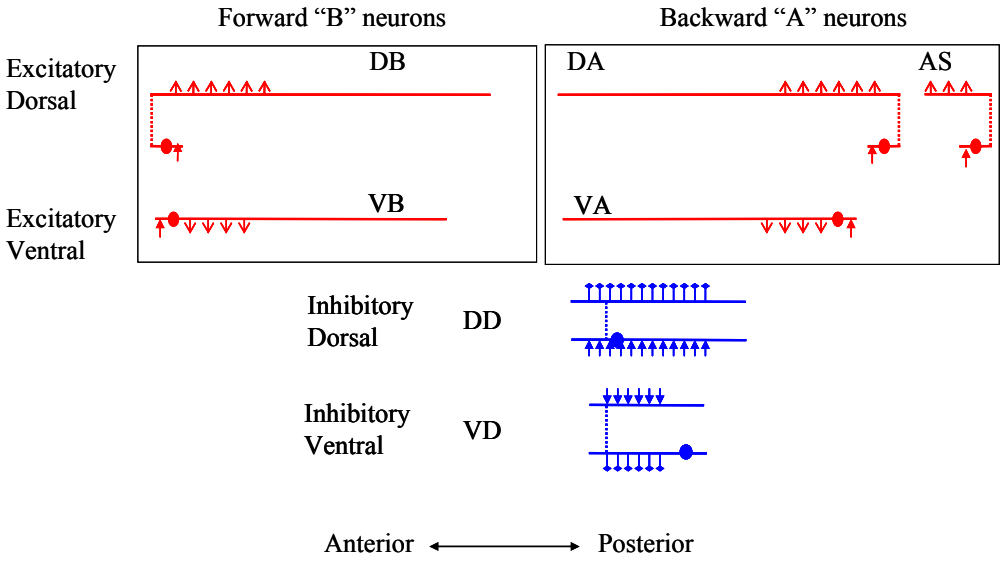

Figure 4.12: Morphology of worm motor neurons. Lines represent neuron processes. Dashed lines indicate position of commissures crossing from ventral to dorsal side of the animal, Solid circles represent neuron cell body. Arrows show typical positions of inputs and outputs. On inhibitory neurons, lines that end in a dot denote inhibitory synaptic output. Diagrams are drawn with worm anterior on the left.

The wiring diagram is a map that charts all the possible ways neurons can communicate with each other. Which paths the signals take depends on a combination of factors internal and external to the animal. In this section, we solved for the dynamical modes or the preferred paths of the forward and backward motor network using a linear model. The results of the computational models are compared to the pattern of activity obtained from imaging experiments.

4.3.2 Representative Motor Unit

To understand the function of the motor circuit, we approximate the wiring diagram as a set of repeating motor "units". These units emerge as repeating segments (gray box in Figure 4.13) in the spatial layouts of the motor neurons and their neuromuscular junctions along the worm. First, we noticed non-overlapping, repeating sets of inhibitory synapses from VD neurons to VA and VB excitatory motor neurons (e.g., VD1 to VA1, VD2 to VA2, and so on). Other connections between motor neurons showed overlap and were more difficult to separate into units. The VD-to-VA/VB neuron pairs thus formed the base of each motor unit. The rest of the motor neurons and their connections are then filled in. Using only fully reconstructed motor neurons that end just anterior to the vulva, we formed 6 units for both forward and backward motor circuits. The trends in connectivity between these units are then distilled down to form a representative forward and backward motor "unit.

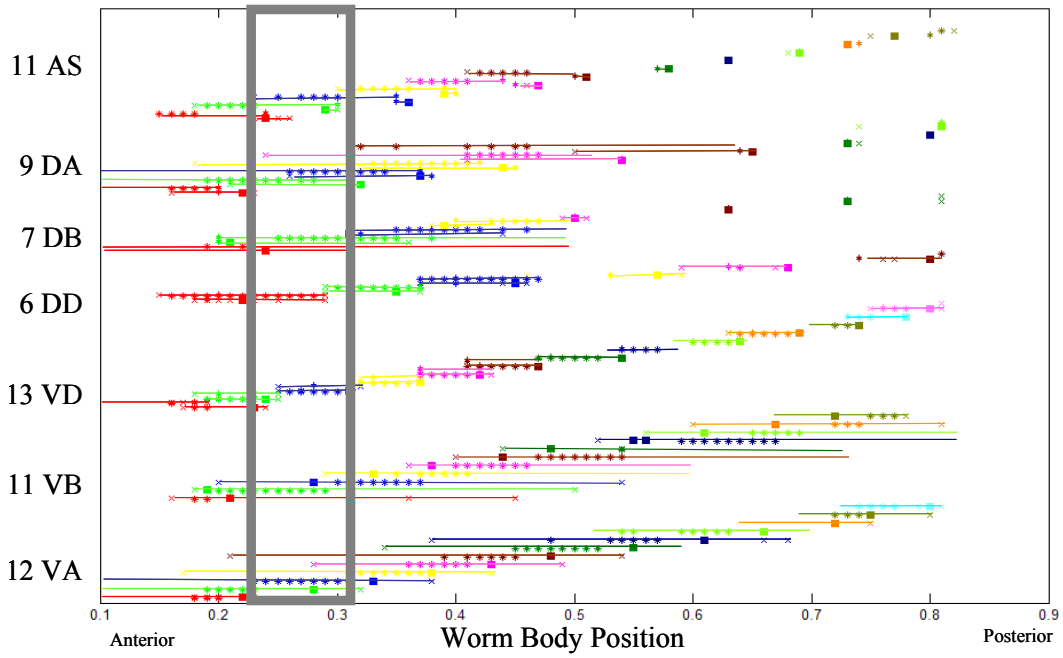

Figure 4.13: Actual spatial layouts of motor neurons. Neurons of each class are drawn according to their positions along the worm. Normalized worm body position is noted on the horizontal axis with 0=head and 1=tail. Each neuron of a given class is shown in a different color to aid the eye. Cell body is denoted by squares and neuromuscular junctions (NMJ) by *. Gray shaded box encloses what appears to be one "unit" in the motor circuit (based on position of NMJ).

Figure 4.14A diagrams the connectivity of the representative forward (B) and backward (A) motor units and their interconnections. Solid lines are connections found in all 6 units in the actual worm whereas dashed lines are present in at least 4 units. Since the actual worm has typically more ventral than dorsal motor neurons (7 DB, 9 DA, 11 AS, 6 DD versus 11 VB, 12 VA, 13VD), the same neuron may appear in more than one unit. Within the forward unit, dorsal excitatory neurons (DB) are consistently connected to both dorsal and ventral inhibitors (DD, VD) while ventral excitatory neurons (VB) always make synapses to DD but not consistently to VD. We also observed synapses from the inhibitory ventral neurons (VD) back to VB, creating a possibly oscillatory inhibition/excitation loop. The coupling between units of the forward locomotive circuit appears to be skewed towards posterior-directed signaling. In addition to gap junctions between inhibitory neurons and DB's across units, the DB's also sometimes send chemical synapses to the adjacent posterior unit. The backward unit contains the same connectivity as the forward circuit but at different frequencies.

However, unlike the coupling of the forward network, the backward units are coupled with an anterior-projecting asymmetry: DA's are wired to the anterior adjacent VD. The "A" circuit also shows consistently repeating gap junctions between AS and VA neurons from every two units.

The *C. elegans* motor network is remarkably similar to that of a large parasitic nematode, *Ascaris suum*. The average *Ascaris* adult is 25 cm long (compared to 1 mm for *C. elegans*) and has around 90 neurons involved in locomotion (Stretton et al. 1985). These neurons can be divided into the familiar 7 classes of ventral and dorsal excitatory/inhibitory neurons found in *C. elegans* (Stretton et al. 1978). Through a combination of anatomical, electrophysiological, and biochemical analysis, researchers have shown the *Ascaris* motor nervous network consists of five repeating units along the anterior-posterior axis (Stretton et al. 1978). Although each motor unit involves 11 motor neurons, the pattern of connectivity between elements in each unit (Fig 4.14B) is quite similar to the representative motor units found *C. elegans* (Stretton et al. 1985). However, other details of the motor circuit, such as connections across units, mechanical-sensory feedback via stretch receptors, and a clear separation between the forward and backward circuits have not been well documented.

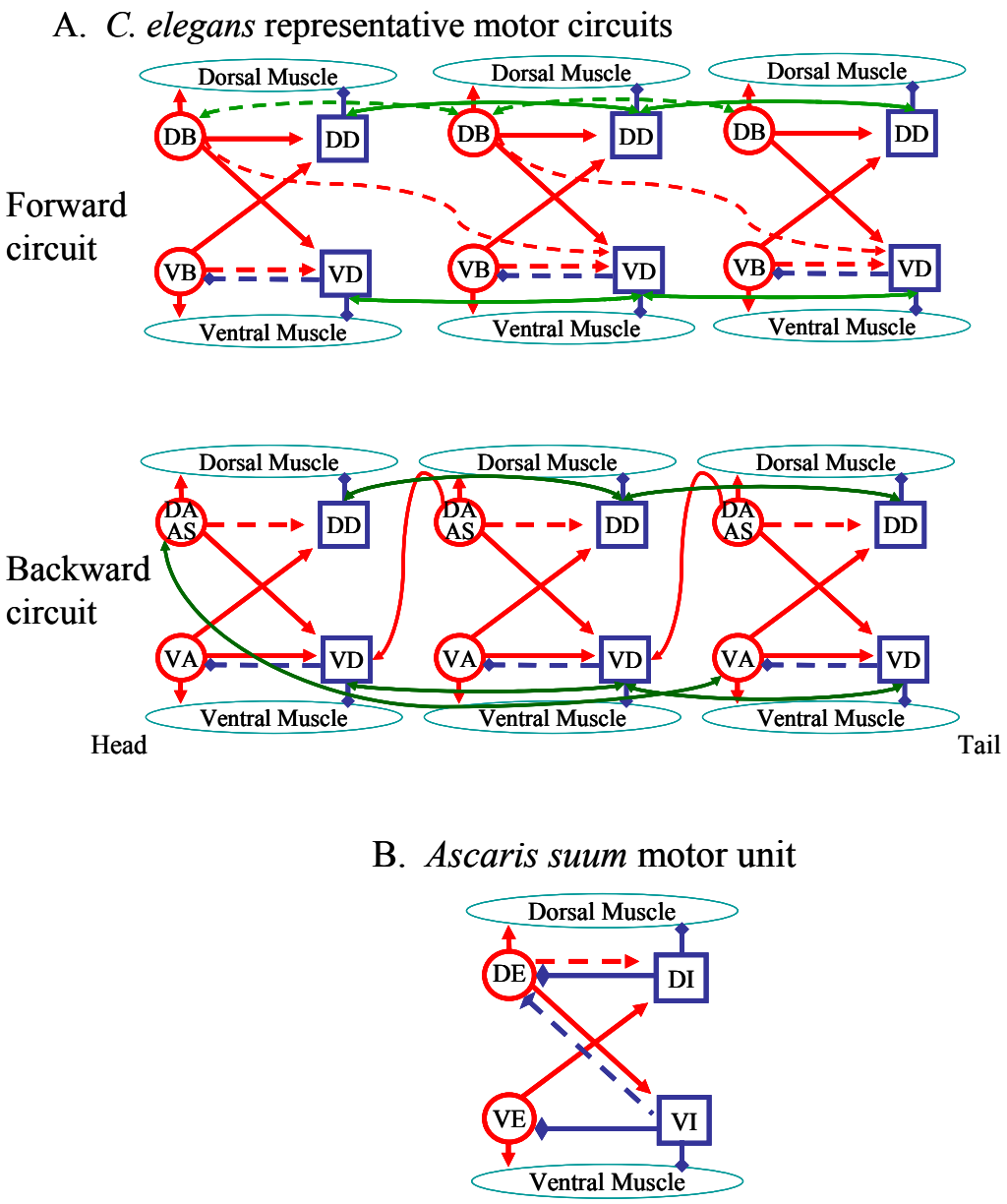

Figure 4.14: **A.** Wiring diagram of *C. elegans* of 3 interconnected units for forward "A" and backward "B" circuits. Solid lines are connections found in 6 of 6 units analyzed in the real circuit while dashed lines appear in at least 4 out of 6 analyzed units. Head is on the left. **B.** Connections between neurons within a single motor unit in *Ascaris suum* (adapted from (Stretton et al. 1985)). DE: dorsal excitatory neuron, DI: dorsal inhibitory neuron, VE: ventral excitatory neuron, VI: ventral inhibitory neuron. Solid lines are connections confirmed by both EM and electrophysiological recordings while dashed lines denote connections found in either EM or cell recordings but not both. **A, B.** Red circles and lines represent synaptic connections from excitatory neurons. Blue squares and lines denote synaptic connections from inhibitory neurons. Green lines indicate bi-directional electrical junctions.

4.3.3 Linear Model of Worm Motor Circuit

Using the representative locomotive circuits from the previous section, we constructed computational models of a separate forward- and backward-motor network, each consisting of 10 corresponding canonical units. *C. elegans* neurons are typically uni- or bi- polar in structure with no distinct axonal or dendritic specialization (White et al. 1986). Instead of classical Na^+-based action potentials, patch-clamp recordings have shown neurons to exhibit graded potentials modulated by voltage-dependent Ca^{2+} and potassium ion (K^+) currents (Goodman et al. 1998; Francis et al. 2003). Furthermore, homologs of voltage-gated Na^+ channels have not been identified in the *C. elegans* genome (Bargmann 1998). Based on the above neuronal properties and the observation that worm neurons are nearly isopotential in steady state (Goodman et al. 1998), we treat each neuron as a single compartment resistive element in an electrical circuit where the time-dependence of voltage (V_i) for a given neuron, i, is the sum of all currents flowing through the cell:

$$C\frac{dV_i}{dt} = -\left(G(V_i - V_o) + \sum_j A_{ij} I_j + I_{ext} \right) \tag{4.3}$$

C is cell capacitance, G is membrane conductance, and V_o is resting potential. The first term on the right-hand-side of Eq. 4.3 represents the leakage current through the membrane. In the second term, I_j is the current injected at a synapse from neuron j, summed over all connected neurons (A_{ij}=±1 if i is connected to j, otherwise A_{ij}=0). Here, unlike the adjacency matrix in Chapter 3 (Eq. 3.2), A is the connectivity matrix defined by the model network and may be asymmetric, i.e., neuron i synapses onto j but not vice versa. Depending on the pre-synaptic neuron, elements of A are either assumed positive (excitatory: DA, AS, VA, DB, VB) or negative (inhibitory: DD, VD). The third term, I_{ext}, consists of current contribution from all non-neuronal elements, such as muscles and sensory signals. In the first-order approximation, we assume input current to be a linear function of voltage ($I_j = \alpha V_j$

where α is a proportionality constant) and that the leakage current is negligibly small (= 0) compared to other terms.

To find properties of the network, we consider contribution from non-neuronal elements (I_{ext}) and make simplifying assumptions to Eq. 4.3. First, we include body muscles into our networks in order to model motor output patterns observed in calcium imaging. For simplicity, they are assumed to have the same electrical properties as neurons where neuromuscular junctions represent inputs. Also, to test the hypothesis of "stretch receptors", we incorporate a "sensory" feedback current which couples the activity of nearby muscles to excitatory motor neurons DA, VA, DB, and VB (connectivity represented by matrix B for neuron i and muscle k). With the above inclusions and simplifications, Eq. 4.3 becomes:

$$\frac{dV_i}{dt} = -\left(\alpha \sum_j A_{ij} V_j + \gamma \sum_k B_{ik} V_k \right) \tag{4.4}$$

V_i is the voltage for the i^{th} neuron or muscle, A_{ij} includes neuron and muscle connectivity, V_k is the voltage of nearby muscle k coupled by B_{ik} (B_{ik}=1 if neuron i is coupled to muscle k, otherwise B_{ik}=0) and the cell capacitance C has been incorporated into constants α and γ.

To get a physical intuition for the "stretch" feedback term in Eq. 4.4, consider the following: The amount of contraction in a muscle cell depends on its depolarization. Since muscles are attached to the worm body, changes in muscle lengths are translated directly to the body. Consistent with the directionality of putative stretch receptors, neurons in the model forward circuit are coupled to muscles in posterior units and vice versa for the backward circuit. The proposed stretch-sensing processes of excitatory motor neurons are between 150 to 350 μm (Chapter 2 and White 1976), covering approximately the length of 2 to 4 muscle cells (typical adult *C. elegans* muscle is 100 μm in length, Hall, *private communications*). In the model, we assume the average of these lengths by coupling stretch feedback across three consecutive anterior/posterior units.

The set of linear equations from Eq. 4.4 (one for each element in the network) can be solved exactly by finding the system's eigenvalues and corresponding eigenvectors. These solutions describe the characteristic patterns of activity, or normal modes, of the system.

4.3.4 Patterns of Muscle Activity from Dominant Modes

To reveal the characteristic patterns of activity during worm locomotion, we solve Eq. 4.4 for all elements in the model forward and backward networks for different stretch couple coefficients ($\gamma = -1, 0, 1$). Since each unit in the forward (backward) model circuit contains 6 (7) elements, a ten-unit network consists of 60 (70) elements, resulting in 60 (70) solutions. Figure 4.15 shows the spectrum of solutions for a 10-unit forward and a 10-unit backward model for negative stretch coupling ($\gamma = -1$) where the imaginary part of the eigenvalue on the vertical axis against the real component on the horizontal axis.

Out of all the dynamical modes of the system, we focus on the dominant oscillatory solution: eigenvalues with the largest positive real part and a nonzero imaginary component. The eigenvalue (λ) gives the time-dependence of activity for each mode (n) and the corresponding eigenvector ($\vec{v}$) provides the weighting factor for each element of the circuit:

$$activity_n = \vec{v}_n e^{\mathrm{Re}\{\lambda_n\}t + i\,\mathrm{Im}\{\lambda_n\}t} \qquad (4.5)$$

From Eq. 4.5, we see that, over time, a positive real eigenvalue will grow exponentially while the imaginary part provides an oscillatory time-dependence. As a result, these modes dominate over the rest of the solutions and are capable of carrying a traveling wave along the worm body. However, if the oscillatory component is much smaller than the real part, i.e. $\mathrm{Im}\{\lambda\} \ll \mathrm{Re}\{\lambda\}$, the amplitude of activity waves would change significantly over a single wavelength of oscillation. Although an exponentially growing solution may seems at first non-biological, such increases could be damped out by the presence of cell leakage currents in the actual animal. For simplicity, we had previously set this value to zero in the model (Eq. 4.4).

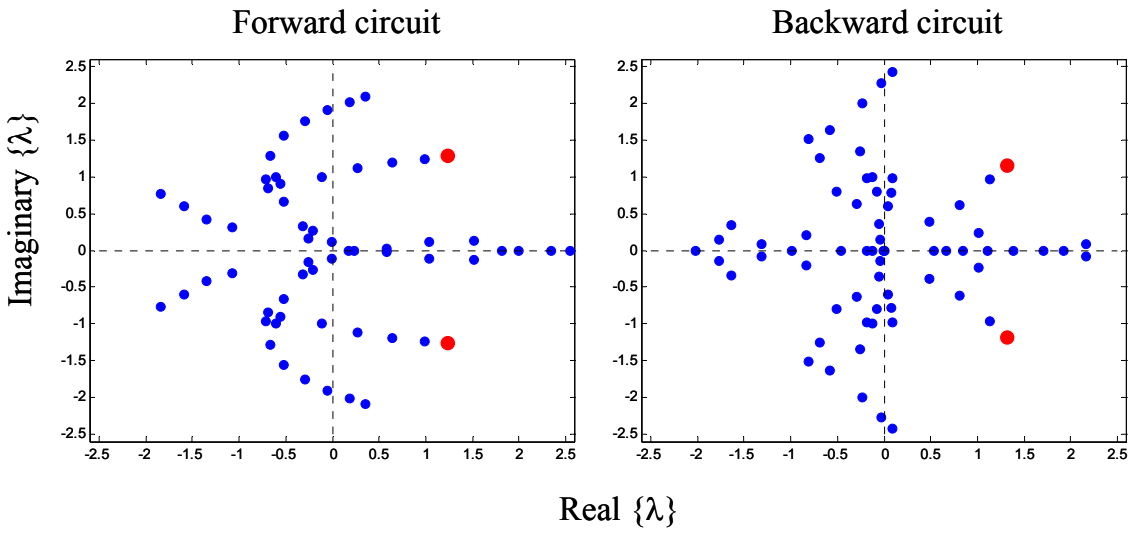

Figure 4.15: Spectrum of solutions for forward and backward linear models. The eigenvalue (λ) of each solution is plotted with imaginary vs. real components. The red dots indicate dominant oscillatory modes.

The dominant solutions of the model network give patterns of muscle activity consistent with observations from calcium imaging. Figure 4.16 (left) shows the phase of body muscle activity for the first oscillatory mode of the forward circuit where the imaginary and real parts of the eigenvalue are of the same order of magnitude (λ=1.24±1.28i), red dots in Fig 4.15 left. This solution is the second largest mode with a nonzero complex eigenvalue, the largest mode has $\mathrm{Im}\{\lambda\} \ll \mathrm{Re}\{\lambda\}$ (see Fig. 4.15). Consistent with the characteristics of a posterior-directed traveling wave, both ventral and dorsal muscles display uniformly increasing phase from head to tail for positive λ with an averaged 3.53 radians phase shift between the two sides of the worm, similar to the π shift observed in imaging experiments. In the backward circuit, the first oscillatory mode gives analogous results for waves traveling towards the head, (λ=1.32±1.16i, dorsal-ventral phase shift: averaged 2.73 radians, Fig. 4.16, right). As a footnote, we found that for coupling values less than -1, the dominant oscillating solution is also the largest oscillating mode. However, we did not fully explore the effects of this parameter.

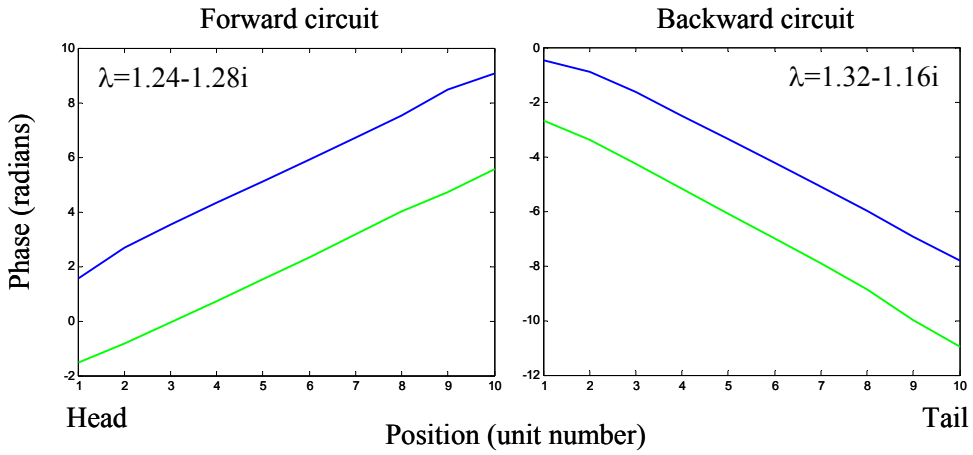

Figure 4.16: Relative phase of muscles in the dominant oscillatory solution. Blue: ventral muscles; Green: dorsal muscles.

We investigate the model's dependence on coupling feedback by setting γ = -1, 0, 1. The patterns of muscle activity for the largest oscillatory modes in the 10-unit backward model circuit are shown in Figure 4.17 bottom (spectrum of solutions is in the top panel). The horizontal axis denotes the unit number or positions along the worm body; the vertical axis represents time in fractions of oscillation cycles; and color represents relative muscle activity. Here, activity of the i^{th} muscle for the n^{th} mode is expressed as a sinusoid with frequency defined by the imaginary part of the eigenvalue (λ) and with amplitude and phase provided by the corresponding eigenvector $\vec{v}$:

$$M_n^i(t) = |v_n(i)| \sin\left(\mathrm{Im}\{\lambda_n\} t + angle(v_n(i))\right) \qquad (4.6)$$

The relative dorsal-ventral phase shift of each solution is shown in the mid panel of Fig 4.17. Without coupling (γ = 0), no muscle waves are present. For positive stretch coupling (γ = 1), muscle waves travel in the same direction compared to the calcium results but the ventral and dorsal sides of the worm are nearly in phase. The solution with negative stretch coupling (γ = -1) gives the only physically-relevant result: a posterior- (anterior-) directed traveling wave for the model forward (backward) circuit with approximately π dorsal-ventral phase shift.

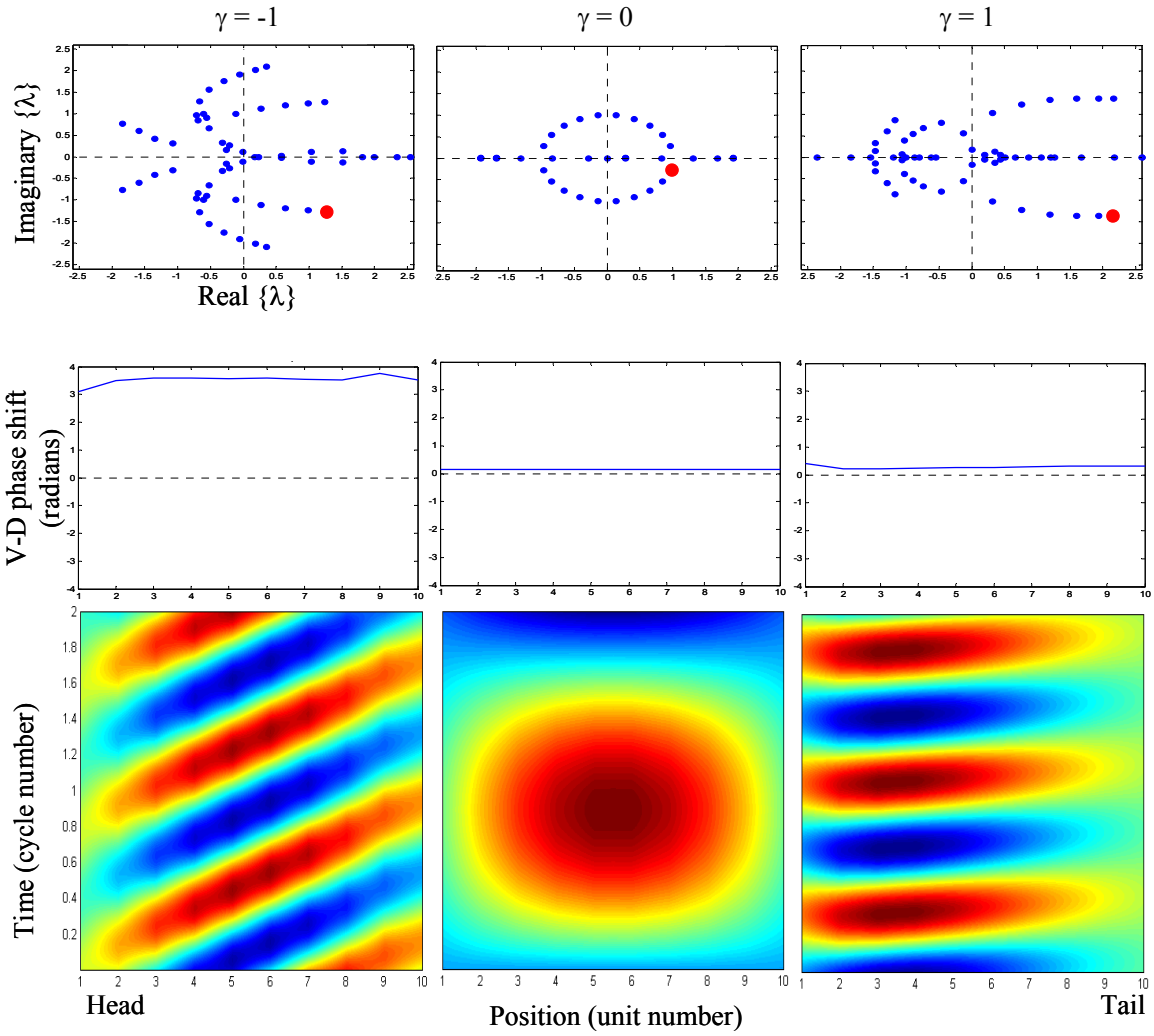

Figure 4.17: Dominant oscillatory solutions of the backward circuit for coupling γ = -1, 0 1. Top: Spectrum of solutions, imaginary vs. real component. Red dot indicates largest oscillatory solution shown in middle and bottom panels. Middle: Ventral-dorsal muscle phase shift. Bottom: Muscle activity patterns. Color denotes relative activity: red = high activity; blue = low activity.

4.3.5 Robustness

We test the robustness of our traveling muscle wave results by systematically removing connections in the model network. To sustain a traveling wave in the experimentally observed direction and dorsal-ventral π phase shift, the model network must contain intra-unit ventral-dorsal cross-inhibition, inter-unit gap junctions between "D" neurons, and negative stretch feedback. This requirement was found in both forward and backward model circuits. Without these connections, no traveling waves were found in oscillatory modes. All other connections can be set to zero without significant changes to the properties of the solution (data not shown).

4.3.6 Discussion

4.3.6.1 Model Network Characterized by Traveling Muscle Waves

Our linear models using *C. elegans's* representative forward and backward motor circuits produced traveling muscle waves consistent with calcium imaging observations: backward waves for the forward circuit and vice versa for backward circuit. These solutions are the largest oscillating modes of the systems, implicating the importance of these characteristics to the properties of the network. In addition to muscle activity, our models also inherently provide activity of motor neurons. With fast-paced advances in calcium imaging of *C. elegans* neurons, perhaps simultaneous recordings from multiple motor neurons will soon be possible. At that time, our model predictions at the neuron level can also be tested in laboratory experiments.

Interestingly, the generation of muscle waves did not require an external or internal oscillating element. Unlike other well studied systems of locomotion, such as the lamprey or leech (Stein et al. 1999), *C. elegans* research has, thus far, produced no evidence of a central pattern generator (CPG) for locomotion. Cell recordings in *Ascaris suum*, a large worm with remarkably similar nervous system, have revealed intrinsic oscillations in inhibitory motor neurons

(equivalent of DD and VD neurons in *C. elegans*, (Davis and Stretton 1989)). However, our model shows that such oscillations are also not required for the network to produce traveling waves.

4.3.6.2 Negative Stretch-Coupling Supports Stretch-Receptor Hypothesis

Using the minimum set of connections necessary to sustain the traveling wave result, the models of forward and backward motion become identical except for the direction of stretch feedback. Both circuits required this stretch coupling to be negative, indicating that motor neurons receive inhibitory signals from active muscles. This result is just another way to describe the "stretch receptor" hypothesis: active muscles which are contracting and short, leads to inhibition of nearby neuron activity versus stretched body leads to excitation of stretch-coupled neurons. With recent progress in electrophysiology and voltage sensitive imaging in worm neurons, perhaps presence of stretch feedback can be directly measured by artificially "stretching" the worm in a controlled manner (Haspel and Hart 2006). The true importance of these "stretch receptors" can be tested in the actual animal by micro-ablating (Yanik et al. 2004) the long process of excitatory motor neurons and observing its effect on worm locomotion.

4.3.6.3 Parameter Space of Our Simple Model Needs To Be Explored

Although our linear model of the worm motor circuit produces muscle waves consistent with experimental observations, many aspects of locomotion remain to be addressed by the simple model. The speed, amplitude and wavelength of muscle waves can be quite different for the same animal moving in different environments. Without fully exploring the parameter space of our model, we cannot conclude whether our model captures some of these wave properties or if they are lost through some of our simplifying assumptions.

In our computation, we have assumed a binary connectivity matrix where the strength of synapses is the same for all elements. The actual worm nervous system contains different number of

synapses between different elements. For example, neuromuscular junctions between a given neuron-muscles pair are typically 1.5-2 times more numerous than synapses between motor neurons (see Chapter 2). With the lack of paired-cell recordings, we cannot truly know the relative strengths of these connections. However, by varying the relative strengths of synapses and neuromuscular junctions in the model, one can potentially make predictions about the importance of synaptic weight.

Another set of unknowns in the model involves the strength and spatial extent of stretch feedback. Experiments have shown that loss of function in putative stretch receptor gene (*unc-8*) produced worms that move with reduced amplitudes (Tavernarakis et al. 1997). This effect can be the result of two scenarios: stretch receptors are not required for undulation or compensation by duplicate stretch receptor genes masks the behavioral phenotype. Again, a reasonable range of coupling strengths should be explored in the model in order to gain insights on the stretch-receptor hypothesis.

Finally, worm literature contains a trove of experiments describing stereotypical changes in locomotive behaviors as a result of mis-wired neurons or non-functional synapses. For example, in animals lacking the orphan nuclear hormone receptor, *unc-55*, ventral inhibitory neurons (VD) adopt the synaptic patterns of their dorsal counterparts (DD), resulting in ventral curling when the worm attempts to move backwards (Zhou and Walthall 1998). In another mutant, instead of having posterior-directed processes, dorsal excitatory neurons (DB) in the forward circuit have anterior-directed processes in animals with non-functional *vab-7*, an *even-skipped*-like homoeodomain protein (Esmaeili et al. 2002). These mutants have normal backward movement but curl up ventrally when induced to move forward. To evaluate how well our computational results represent the actual worm, our model will have to be tested against these mutant scenarios.

4.3.7 Conclusion

Using linear models of the worm's representative motor circuits, we found large dynamical modes of the network to be consistent with observed muscle patterns from calcium imaging: forward circuit characterized by backward-traveling muscle waves and vice versa for the backward circuit. Unlike other well-studied systems, the waves of activity along the worm body did not require the presence of intrinsic or extrinsic central pattern generators. Instead, these results depend on negative feedback from muscles to excitatory motor neurons in a direction consistent with the hypothesis that asymmetrically directed neural projections contain stretch receptors. Although the results of our linear model are compelling, much more work still needs to be done to explore the limits of the simple network and its ability to describe worm locomotion. We believe some of the predictions from the model, such as the requirement of stretch-feedback and, soon, the activity of motor neurons, can be tested in a laboratory setting.

Chapter 5: Conclusion

In the current study, we explored the relationship between neuronal structure and function/ behavior in the nematode, *Caenorhabditis elegans*. We first established a firm base for our work by compiling an updated version of the worm neuronal connectivity network that is now 95% complete. Then, using the new wiring diagram, we solved for the neuronal layout of the entire nervous system based on the hypothesis that neuronal placement in animals minimizes wiring cost specified by synaptic connectivity. In the optimal layout, most neurons are located close to their actual positions, suggesting wiring minimization as an important constraint in the organization of neurons in the worm. Some neurons that deviated strongly from their "optimal" positions were found to play specific roles in the worm nervous system relating to axonal guidance and command neuron functions. We also used the wiring diagram to study the dynamical properties of the worm motor network and compared the results to actual patterns of muscle activity during worm locomotion. By performing calcium imaging of body-wall muscles in moving worms, we described stereotypical patterns of muscle activity and explored the relationship between worm propulsive forces and body shape. Using linear models of the worm's representative forward and backward motor circuits, we found large dynamical modes of the system to be consistent with observed muscle patterns. These results did not require an intrinsic or external pattern generator but depended on a muscle-to-neuron negative feedback as proposed in the stretch receptor hypothesis. In short, we used the wiring diagram to gain insights on the worm nervous system's design and function and found that locomotive behaviors are intrinsic properties of the neuronal circuitry.

Much more is still to be learned from the neuronal network of *C. elegans*. For the current work, we tackled a very simple, spontaneous behavior of forward and backward locomotion. The natural next step would be to investigate evoked behavior such as worm response to touch or chemosensory stimuli. The results would further our understanding of how specific neural wiring patterns contribute to processing of external stimuli and elicitation of responses. We hope that,

through the success of predicting neuronal function and animal behavior from the wiring diagram of this simple nervous system, we will gain knowledge on the neural correlate of behavior for more complex animals.

References

Achacoso, T.B. and W.S. Yamamoto. 1992. *AY's Neuroanatomy of C. elegans for Computation*. CRC Press, Boca Raton.

Ackley, B.D. and Y. Jin. 2004. Genetic analysis of synaptic target recognition and assembly. *Trends Neurosci* 27: 540-7.

Alberts, B., A. Johnson, J. Lewis, M. Raff, K. Roberts, and P. Walter. 2002. *Molecular Biology of the Cell*. Garland Science.

Altun, Z.F. and D.H. Hall. 2002-2006. WormAtlas. http://www.wormatlas.org.

Ambros, V. 2006. Worm Methods. *WormBook* ed. The *C. elegans* Research Community: doi/10.1895/wormbook, http://www.wormbook.org.

Antebi, A., C. Norris, E. Hedgecock, and G. Garriga. 1997. Cell and growth cone migrations. In *C. Elegans II*. Cold Spring Harbor Laboratory Press.

Attwell, D. and S.B. Laughlin. 2001. An energy budget for signaling in the grey matter of the brain. *J Cereb Blood Flow Metab* 21: 1133-45.

Aurelio, O., D.H. Hall, and O. Hobert. 2002. Immunoglobulin-domain proteins required for maintenance of ventral nerve cord organization. *Science* 295: 686-90.

Bargmann, C.I. 1998. Neurobiology of the *Caenorhabditis elegans* genome. *Science* 282: 2028-2033.

Braitenberg, V. and R.P. Atwood. 1958. Morphological observations on the cerebellar cortex. *J. Comp. Neurol.* 109: 1-34.

Bray, D. 1979. Mechanical tension produced by nerve cells in tissue culture. *J Cell Sci* 37: 391-410.

Brenner, S. 1988. In *The Nematode Caenorhabditis elegans* (ed. W. Wood). Cold Spring Harbor Laboratory Press, Cold Spring Harbor.

Bryden, J. 2003. A simulation model of the locomotion controllers for the nematode *Caenorhabditis elegans*. In *School of Computing Biosystems*, pp. 98. University of Leeds, Leeds.

Cacciatore, T.W., R. Rozenshteyn, and W.B. Kristan Jr. 2000. Kinematics and modeling of leech crawling: evidence for an oscillatory behavior produced by propagating waves of excitation. *Journal of Neuroscience* 20: 1643-1655.

Carroll, S.B. 2005. *Endless Forms Most Beautiful*. W. W. Norton & Company.

Chalfie, M. 1993. Homeobox genes in *Caenorhabditis elegans*. *Curr Opin Genet Dev* 3: 275-277.

Chalfie, M., J.E. Sulston, J.G. White, E. Southgate, J.N. Thomson, and S. Brenner. 1985. The neural circuit for touch sensitivity in Caenorhabditis elegans. *J Neurosci* 5: 956-64.

Chalfie, M. and J.G. White. 1988. The Nervous System. In *The nematode Caenorhabditis elegans* (ed. W. Wood), pp. 337-392. Cold Spring Harbor Laboratory Press, Cold Spring Harbor.

Cherniak, C. 1992. Local optimization of neuron arbors. *Biol Cybern* 66: 503-10.

-. 1994. Component placement optimization in the brain. *J Neurosci* 14: 2418-27.

-. 1995. Neural component placement. *Trends Neurosci* 18: 522-7.

Chklovskii, D.B. 2000a. Binocular disparity can explain the orientation of ocular dominance stripes in primate primary visual area (V1). *Vision Res* 40: 1765-73.

-. 2000b. Optimal sizes of dendritic and axonal arbors in a topographic projection. *J Neurophysiol* 83: 2113-9.

-. 2004a. Exact solution for the optimal neuronal layout problem. *Neural Comput* 16: 2067-78.

-. 2004b. Synaptic connectivity and neuronal morphology: two sides of the same coin. *Neuron* 43: 609-17.

Chklovskii, D.B. and A.A. Koulakov. 2000. A wire length minimization approach to ocular dominance patterns in mammalian visual cortex. *Physica A* 284: 318-334.

-. 2004. Maps in the brain: what can we learn from them? *Annu Rev Neurosci* 27: 369-92.

Christensen, M., A. Estevez, X. Yin, R. Fox, R. Morrison, M. McDonnell, C. Gleason, D.M. Miller, and K. Strange. 2002. A primary culture system for functional analysis of *C. elegans* neurons and muscle cells. *Neuron* 33: 503-514.

Cline, H. 2005. Synaptogenesis: a balancing act between excitation and inhibition. *Curr Biol* 15: R203-5.

Condron, B.G. and K. Zinn. 1997. Regulated neurite tension as a mechanism for determination of neuronal arbor geometries in vivo. *Curr Biol* 7: 813-6.

Croll, N.A. 1975. Components and patterns in the behaviour of the nematode *Caenorhabditis elegans*. *J. Zool. Lond* 176: 159-176.

Culotti, J.G. and D.C. Merz. 1998. DCC and netrins. *Curr Opin Cell Biol* 10: 609-13.

Davis, R.E. and A.O.W. Stretton. 1989. Signaling properties of *Ascaris* motorneurons: graded active responses, graded synaptic transmission, and tonic transmitter release. *Journal of Neuroscience* 9: 415-425.

Dickson, B.J. 2002. Molecular mechanisms of axon guidance. *Science* 298: 1959-64.

Dixon, S.J. and P.J. Roy. 2005. Muscle arm development in Caenorhabditis elegans. *Development* 132: 3079-3092.

Driscoll, M. and J. Kaplan. 1997. Mechanotransduction. In *C. Elegans II*. Cold Spring Harbor Press.

Dunn, N.A., S.R. Lockery, J.T. Pierce-Shimomura, and J.S. Conery. 2004. A neural network model of chemotaxis predicts functions of synaptic connections in the nematode *Caenorhabditis elegans*. *J Comput Neurosci* 17: 137-147.

Durbin, R.M. 1987. Studies on the Development and Organisation of the Nervous System of Caenorhabditis elegans. In. Cambride University, Cambridge.

Erdös, P. and E. Niebur. 1990. The neural basis of the locomotion of nematodes. In *Statistical Mechanics of Neural Networks* (ed. L. Garrido), pp. 253-267. Springer-Verlag Berlin, Heidelberg.

Esmaeili, B., J.M. Ross, C. Neades, D.M. Miller, and J. Ahringer. 2002. The *C. elegans even-skipped* homologue, *vab-7*, specifies DB motoneurone identity and axon trajectory. *Development* 129: 853-862.

Ferrée, T.C. and S.R. Lockery. 2001. Computational rules for chemotaxis in the nematode *C. elegans*. *J. Comp. Neurosci.* 6: 263-277.

Francis, G.R. and R.H. Waterston. 1985. Muscle organization in *Caenorhabditis elegans*: localization of proteins implicated in thin filament attachment and I-band organization. *J. Cell Biol.* 101: 1532-1549.

Francis, M.M., J.E. Mellem, and A.V. Maricq. 2003. Bridging the gap between genes and behavior: recent advances in the electrophysiological analysis of neural function in *Caenorhabditis elegans*. *Trends Neurosci* 26: 90-99.

Fukata, M., M. Nakagawa, and K. Kaibuchi. 2003. Roles of Rho-family GTPases in cell polarisation and directional migration. *Curr Opin Cell Biol* 15: 590-7.

Goodman, M.B., D.H. Hall, L. Avery, and S.R. Lockery. 1998. Active currents regulate sensitivity and dynamic range in C. elegans neurons. *Neuron* 20: 763-72.

Gray, J. 1953. Undulatory Propulsion. *Quarterly Journal of Microscopical Sciences* 94: 551-578.

Gray, J. and H.W. Lissmann. 1964. The locomotion of nematodes. *J Exp Biol.* 41: 135-154.

Grillner, S., O. Ekeberg, A. El Manira, A. Lansner, D. Parker, J. Tegner, and P. Wallen. 1998. Intrinsic function of a neuronal network - a vertebrate central pattern generator. *Brain Research Reviews* 26: 184-197.

Hall, D.H. and R.L. Russell. 1991. The posterior nervous system of the nematode Caenorhabditis elegans: serial reconstruction of identified neurons and complete pattern of synaptic interactions. *J Neurosci* 11: 1-22.

Hall, K. 1970. An r-dimensional quadratic placement algorithm. *Management Science* 17: 219-229.

Hamelin, M., Y. Zhou, M.W. Su, I.M. Scott, and J.G. Culotti. 1993. Expression of the UNC-5 guidance receptor in the touch neurons of C. elegans steers their axons dorsally. *Nature* 364: 327-30.

Haspel, G. and A. Hart. 2006. Stretch Receptors and Pattern Generation in *C. elegans* Locomotion Circuit. In *C. elegans Neuronal Development, Synaptic Function, and Behavior Meeting*, Madison, WI.

Hedgecock, E.M., J.G. Culotti, D.H. Hall, and B.D. Stern. 1987. Genetics of cell and axon migrations in Caenorhabditis elegans. *Development* 100: 365-82.

Hobert, O. 2005. Specification of the nervous system. *WormBook* ed. The *C. elegans* Research Community: doi/10.1895/wormbook.1.12.1, http://www.wormbook.org.

Jin, Y. 2005. Synaptogenesis. *WormBook* ed. The *C. elegans* Research Community: doi/10.1895/wormbook.1.44.1,http://www.wormbook.org.

Jin, Y., E. Jorgensen, E. Hartwieg, and H.R. Horvitz. 1999. The *Caenorhabditis elegans* gene unc-25 encodes glutamic acid decarboxylase and is required for synaptic transmission but not synaptic development. *J Neurosci* 19: 539-548.

Jospin, M., V. Jacquemond, M.-C. Mariol, L. Segalat, and B. Allard. 2002. The L-type voltage-dependent Ca^{2+} channel EGL-19 controls body wall muscle function in *Caenorhabditis elegans*. *Journal of Cell Biology* 159: 337-347.

Karbowski, J., C.J. Cronin, A. Seah, J.E. Mendel, D. Cleary, and P.W. Sternberg. 2006. Conservation rules, their breakdown, and optimality in *Caenorhabditis* sinusoidal locomotion. *J Theor Biol.* 242: 652-669.

Kennings, A. and I. Markov. 2000. Analytical Minimization of Half-Perimeter Wirelength. In *IEEE/ACM Asia and South Pacific Design Automation Conference*, pp. 179-184.

Kerr, R., V. Lev-Ram, G. Baird, P. Vincent, R.Y. Tsien, and W.R. Schafer. 2000. Optical imaging of calcium transients in neurons and pharyngeal muscles of *C. elegans*. *Neuron* 26: 583-594.

Klyachko, V.A. and C.F. Stevens. 2003. Connectivity optimization and the positioning of cortical areas. *Proc Natl Acad Sci U S A* 100: 7937-41.

Laughlin, S.B., R.R. de Ruyter van Steveninck, and J.C. Anderson. 1998. The metabolic cost of neural information. *Nat Neurosci* 1: 36-41.

Lewis, J.A., C.H. Wu, J.H. Levine, and H. Berg. 1980. Levamisole-resistant mutants of the nematode *Caenorhabditis elegans* appear to lack pharmacological acetylcholine receptors. *Neuroscience* 5: 967-989.

Liu, q., B. Chen, E. Gaier, J. Joshi, and Z.W. Wang. 2006. Low-conductance gap junctions mediate specific elecrical coupling in body-wall muscle cells of *C. elegans*. *J Biol Bhem.* 281: 7881-7889.

Lockery, S.R. and T.J. Sejnowski. 1993. The computational leech. *Trends Neurosci* 16: 283-290.

Marder, E. and R.L. Calabrese. 1996. Principles of rhythmic motor pattern generation. *Physiol. Rev.* 76: 687-717.

Maryon, E.B., B. Saari, and P. Anderson. 1998. Muscle-specific function of ryanodine receptor channels in *Caenorhabditis elegans*. *J Cell Sci* 111: 2885-2895.

McIntire, S.L., E. Jorgensen, J. Kaplan, and H.R. Horvitz. 1993a. The GABAergic nervous system of Caenorhabditis elegans. *Nature* 364: 337-41.

-. 1993b. The GABAergic nervous system of *Caenorhabditis elegans*. *Nature* 364: 334-337.

Mitchison, G. 1991. Neuronal branching patterns and the economy of cortical wiring. *Proc R Soc Lond B Biol Sci* 245: 151-8.

Miyawaki, A., J. Llopis, R. Heim, J.M. McCaffery, J.A. Adams, M. Ikura, and R.Y. Tsien. 1997. Fluorescent indicators for Ca^{2+} based on green fluorescent proteins and calmodulin. *Nature* 388: 882-887.

Niebur, E. and P. Erdös. 1991. Theory of the locomotion of nematodes: Dynamics of undulatory progression on a surface. *J. Biophys.* 60: 1132-1146.

-. 1993a. Modeling locomotion and its neural control in nematodes. *Comments on Theoretical Biology* 3: 109-139.

-. 1993b. Theory of Locomotion of Nematodes: Control of the Somatic Motor Neurons by Interneurons. *Mathematical Biosciences* 118: 51-82.

Okkema, P.G., S.W. Harrison, V. Plunger, A. Aryana, and A. Fire. 1993. Sequence requirements for myosin gene expression and regulation in *Caenorhabditis elegans*. *Genetics* 135: 385-404.

Parker, G. and J. Maynard Smith. 1990. Optimality theory in evolutionary biology. *Nature* 348: 27-33.

Pierce-Shimomura, J.T., M. Dores, and S.R. Lockery. 2005. Analysis of the effects of turning bias on chemotaxis in *C. elegans*. *Journal of Experimental Biology* 208: 4727-4733.

Rall, W., R.E. Burke, W.R. Holmes, J.J. Jack, S.J. Redman, and I. Segev. 1992. Matching dendritic neuron models to experimental data. *Physiol Rev* 72: S159-86.

Ramón y Cajal, S. 1899. *Textura del Sistema Nervioso del Hombre y de los Vertebrados. Translation: Texture of the Nervous System of Man and the Vertebrates*. Springer, 1999, New-York.

Ren, X.C., S. Kim, E. Fox, E.M. Hedgecock, and W.G. Wadsworth. 1999. Role of netrin UNC-6 in patterning the longitudinal nerves of Caenorhabditis elegans. *J Neurobiol* 39: 107-18.

Richmond, J.E. and E. Jorgensen. 1999. One GABA and two acetylcholine receptors function at the *C. elegans* neuromuscular junction. *Nat Neurosci* 2: 791-797.

Rushton, W.A. 1951. Theory of the effects of fibre size in medullated nerve. *J Physiol* 115: 101-122.

Sakata, K. and R. Shingai. 2004. Neural network model to generate head swing in locomotion of *Caenorhabditis elegans*. *Network: Computation in Neural Systems* 15: 199-216.

Shefi, O., A. Harel, D.B. Chklovskii, E. Ben Jacob, and A. Ayali. 2003. Biophysical constraints on neuronal branching. *Neurocomputing* 58-60: 487-495.

Shen, K. and C.I. Bargmann. 2003. The immunoglobulin superfamily protein SYG-1 determines the location of specific synapses in C. elegans. *Cell* 112: 619-30.

Shyn, S.I., R. Kerr, and W.R. Schafer. 2003. Serotonin and Go modulate functional states of neurons and muscles controlling *C. elegans* egg-laying behavior. *Curr Biol* 13: 1910-1915.

Sigl, G., D. K, and F. Johannes. 1991. Analytical placement: a linear or quadratic objective function? In *Proc. ACM/IEEE Design Automation Conf.*, pp. 57-62.

Starovasnik, M.A., D.R. Su, K. Beckingham, and R.E. Klevit. 1992. A series of point mutations reveal interactions between the calcium-binding sites of calmodulin. *Protein Science* 1: 245-253.

Stein, P.S.G., S. Grillner, A.I. Selverston, and D.G. Stuart. 1999. *Neurons, networks, and motor behavior*. MIT Press, Cambridge, MA.

Stretton, A.O.W., R.E. Davis, J.D. Angstadt, J.E. Donmoyer, and C.D. Johnson. 1985. Neural control of behaviour in *Ascaris*. *Trends Neurosci* 8: 294-300.

Stretton, A.O.W., R.M. Fishpool, E. Southgate, J.E. Donmoyer, J.E.R. Moses, J.P. Walrond, and I.S. Kass. 1978. Structure and physiolocial activity of the motorneurons of the nematode *Ascaris*. *Proc Natl Acad Sci U S A* 75: 3493-3497.

Sulston, J.E. 1976. Post-embryonic development in the ventral cord of Caenorhabditis elegans. *Philos Trans R Soc Lond B Biol Sci* 275: 287-97.

Sulston, J.E. and H.R. Horvitz. 1977. Post-embryonic cell lineages of the nematode, Caenorhabditis elegans. *Dev Biol* 56: 110-56.

Sulston, J.E., E. Schierenberg, J.G. White, and J.N. Thomson. 1983. The embryonic cell lineage of the nematode Caenorhabditis elegans. *Dev Biol* 100: 64-119.

Suzuki, H., R. Kerr, L. Bianchi, C. Frokjaer-Jensen, D. Slone, J. Xue, B. Gerstbrein, M. Driscoll, and W.R. Schafer. 2003. In vivo imaging of *C. elegans* mechanosensory neurons demonstrates a specific role for the MEC-4 channel in the process of gentle touch sensation. *Neuron* 39: 1005-17.

Tavernarakis, N., W. Shreffler, S. Wang, and M. Driscoll. 1997. unc-8, a DEG/ENaC family member, encodes a subunit of a candidate mechanically gated channel that modulates *C. elegans* locomotion. *Neuron* 18: 107-19.

Tessier-Lavigne, M. and C.S. Goodman. 1996. The molecular biology of axon guidance. *Science* 274: 1123-33.

Tsay, R. and E. Kuh. 1991. A unified approach to partitioning and placement. *IEEE Transactions on Circuits and Systems* 38: 521-533.

Van Essen, D.C. 1997. A tension-based theory of morphogenesis and compact wiring in the central nervous system. *Nature* 385: 313-8.

Wadsworth, W.G. and E.M. Hedgecock. 1992. Guidance of neuroblast migrations and axonal projections in *Caenorhabditis elegans*. *Curr Opin Neurobiol* 2: 36-41.

Wallace, H.R. 1968. The dynamics of nematode movement. *Annual Reviews of Phytopathology* 6: 91-114.

Ward, S., J.N. Thomson, J.G. White, and S. Brenner. 1975. Electron microscopical reconstruction of the anterior sensory anatomy of the nematode *Caenorhabditis elegans*. *J. Comp. Neurol.* 160.

Ware, R.W., D. Clark, K. Crossland, and R.L. Russell. 1975. The nerve ring of the nematode *Caenorhabditis elegans*: Sensory input and motor output. *J. Comp. Neurol.* 162.

Weis, B. and D. Mlynski. 1987. A new relative placement procedure based on mSST and linear programming. In *Proc. IEEE Int. Symp. on Circuits and Systems*, pp. 564-567.

Wen, Q. and D.B. Chklovskii. 2005. Segregation of the brain into gray and white matter: a design minimizing conduction delays. *PLoS Comput Biol* 1: e78.

White, J.G., E. Southgate, and J.N. Thomson. 1992. Mutations in the Caenorhabditis elegans unc-4 gene alter the synaptic input to ventral cord motor neurons. *Nature* 355: 838-41.

White, J.G., E. Southgate, J.N. Thomson, and S. Brenner. 1976. The structure of the ventral nerve cord of *Caenorhabditis elegans*. *Philos Trans R Soc Lond B Biol Sci* 275: 327-348.

-. 1986. The structure of the nervous system of the nematode Caenorhabditis elegans. *Philos. Trans. R. Soc. Lond. B Biol. Sci.* 314: 1-340.

Wicks, S.R. and C.H. Rankin. 1995. Integration of mechanosensory stimuli in Caenorhabditis elegans. *J Neurosci* 15: 2434-44.

Wicks, S.R., C.J. Roehrig, and C.H. Rankin. 1996. A dynamic network simulation of the nematode tap withdrawal circuit: predictions concerning synaptic function using behavioral criteria. *Journal of Neuroscience* 16: 4017-4031.

Williams, T.L. 1989. Locomotion in lamprey and trout: the relative timing of activation and movement. *Journal of Experimental Biology* 143: 559-566.

Yanik, M.F., H. Cinar, H.N. Cinar, A.D. Chisholm, Y. Jin, and A. Ben-Yakar. 2004. Functional regeneration after laser axotomy. *Nature* 432: 822.

Young, M.P. and J.W. Scannell. 1996. Component-placement optimization in the brain. *Trends Neurosci* 19: 413-5.

Zhao, B., P. Khare, L. Feldman, and J.A. Dent. 2003. Reversal frequency in *Caenorhabditis elegans* represents an integrated response to the state of the animal and its environment. *Journal of Neuroscience* 23: 5319-5328.

Zheng, M., W.O. Friesen, and T. Iwasaki. 2007. Systems-level modeling of neuronal circuits for leech swimming. *J. Comput Neurosci* 22: 21-38.

Zhou, H.M. and W.W. Walthall. 1998. *UNC-55*, an orphan nuclear hormone receptor, orchestrates synaptic specificity among two classes of motor neurons in *Caenorhabditis elegans*. *J Neurosci* 18: 10438-44.